Effects of pellet-sinter interaction parameters on component segregation and bed porosity considering flow velocity and mixture composition

A DEM study

Roeplal, Raïsa; Pang, Yusong; Schott, Dingena

DOI
10.1016/j.apt.2023.104322

Publication date
2024

Document Version
Final published version

Published in
Advanced Powder Technology

Citation (APA)
Roeplal, R., Pang, Y., & Schott, D. (2024). Effects of pellet-sinter interaction parameters on component segregation and bed porosity considering flow velocity and mixture composition: A DEM study. *Advanced Powder Technology*, *35*(2), Article 104322. https://doi.org/10.1016/j.apt.2023.104322

Advanced Powder Technology 35 (2024) 104322

Contents lists available at ScienceDirect

Advanced Powder Technology

journal homepage: www.elsevier.com/locate/apt

Effects of pellet-sinter interaction parameters on component segregation and bed porosity considering flow velocity and mixture composition: A DEM study

Raïsa Roeplal *, Yusong Pang, Dingena Schott

TU Delft, Mekelweg 2 2628 CD, Delft, the Netherlands

ARTICLE INFO

Article history:
Received 21 August 2023
Received in revised form 21 December 2023
Accepted 27 December 2023
Available online xxxx

Keywords:
Blast furnace mixture
Component segregation
Porosity
Interaction parameters
Sensitivity analysis
DEM

ABSTRACT

Bed permeability is a crucial factor in blast furnace performance which depends on the material distribution achieved through charging. Since a homogeneous bed of pellet and sinter is recommended, it is crucial to understand whether segregation of the pellet-sinter mixture occurs during charging. The Discrete Element Method is useful in this regard; however, simulations of pellet-sinter mixture charging currently lack credibility since pellet-sinter interaction parameters have not yet been calibrated and validated. Determining pellet-sinter interaction parameters will require significant efforts, so it is useful to know whether mixture segregation and the resulting bed permeability are sensitive to these parameters. In this work, we investigate to what extent the restitution coefficient, sliding friction coefficient and rolling friction coefficient between pellet and sinter affect segregation during bed formation and the resulting permeability in terms of porosity using a simplified charging setup. The investigation is done for different mixture compositions and flow velocities, and analysis settings including sample size and sampling directions. We conclude that all parameters affect segregation and porosity, regardless of the composition and velocity. Hence, all mixture parameters including the interaction parameters between the components must be carefully calibrated when developing a model for predicting permeability.

1. Introduction

Steel is the most widely used engineering and construction material worldwide. In blast furnace steelmaking, liquid iron is extracted from a mixture of ferrous materials (ores), which are generally pellet, sinter and lump ore, and subsequently refined to steel. At the beginning of the process, alternating layers of coke and the ferrous mixture are charged to the furnace to form a packed bed of solids. Next, a pressurized blast of hot gas is injected at the bottom of the furnace. The gas reacts with the bed of particles as it ascends towards the top of the furnace. Consequently, the iron encapsulated in the ferrous particles starts to melt and the molten iron is collected at the bottom of the furnace. Given the global demand for steel products, it is important to optimize the iron extraction process in terms of cost, energy consumption and carbon emissions.

For many years, researchers have pointed out that the permeability distribution of the packed bed determines the efficiency of iron extraction process [1,2,3,4,5,6]. The permeability generally depends on the bed configuration, *i.e.*, on how different materials are arranged after being charged. For the ferrous layer in particular, having an even distribution of the different ores is good practice with respect to the layer's permeability [7]. However, the ore mixture is expected to segregate during charging since the pellet, sinter and lump ore differ in particle size, shape and density. This potentially impedes the achievement of a homogeneous component distribution, which may affect the ore layer's permeability. Therefore, it is required to get insight in the component distribution achieved through current charging practices as a first step towards process optimization. Unfortunately, the harsh operational conditions in a blast furnace hinder observing and measuring the material distribution in practice.

---

* Corresponding author.
E-mail address: r.n.roeplal@tudelft.nl (R. Roeplal).

https://doi.org/10.1016/j.apt.2023.104322
0921-8831/

A lot of research in this field encompasses developing computational models for predicting and optimizing the material distribution after charging in terms of permeability. The Discrete Element Method (DEM) [8] holds great potential for this purpose since it allows the position of each individual grain in the material to be calculated over time and can therefore provide detailed information of the material distribution. When developing a DEM model for a specific material, the interaction between particles and their surroundings must be defined through contact model parameters, also referred to as “interaction parameters”. As shown in Fig. 1, a complete blast furnace model requires the interaction parameters between individual materials and different materials to be defined. These parameters can be determined through experimental characterization, bulk calibration, or a combination of thereof. In our literature review [7] we showed that the Hertz-Mindlin contact model [9] and rolling model C [10] are typically used together in the blast furnace context, and that the current literature has two main shortcomings when it comes to the corresponding interaction parameters (restitution coefficient *e*, sliding friction coefficient μ_s, and rolling friction coefficient μ_r). The first is that the interaction parameters between different materials have not yet been calibrated. While there are several studies on blast furnace charging using pellet-sinter mixtures [11,12,13,14,15,16], the interaction parameters between pellet and sinter were assumed rather than determined in these studies. Although the interaction parameters for individual materials have been calibrated previously (*e.g.*, in [17,18,19,20,21]), the small-scale calibration experiments used to determine the interaction parameters fail to produce relatively high blast furnace flow velocities (in the order of 10 m/s at the lowest chute angle, as illustrated in Fig. 1). Due to this second shortcoming, even the calibrated models in literature currently lack credibility. Hence, blast furnace mixture calibration is expected to be a topic of investigation in the coming years. As we stated in [7], sensitivity analyses are recommended as a first step to avoid a lengthy calibration process.

The objective of this work is to identify the effect of pellet-sinter interaction parameters on bed homogeneity and permeability by means of sensitivity analyses. Rather than using a full-scale blast furnace for this investigation, we form a packed bed by means of a simplified setup which allows for relatively fast simulation runs. Although the system is smaller than a full-scale blast furnace, we ensure that a representative flow velocity is reached. Since this velocity is achieved at the lowest chute angle (*i.e.*, when the flow is nearly vertical) in blast furnace operations, our simplified setup

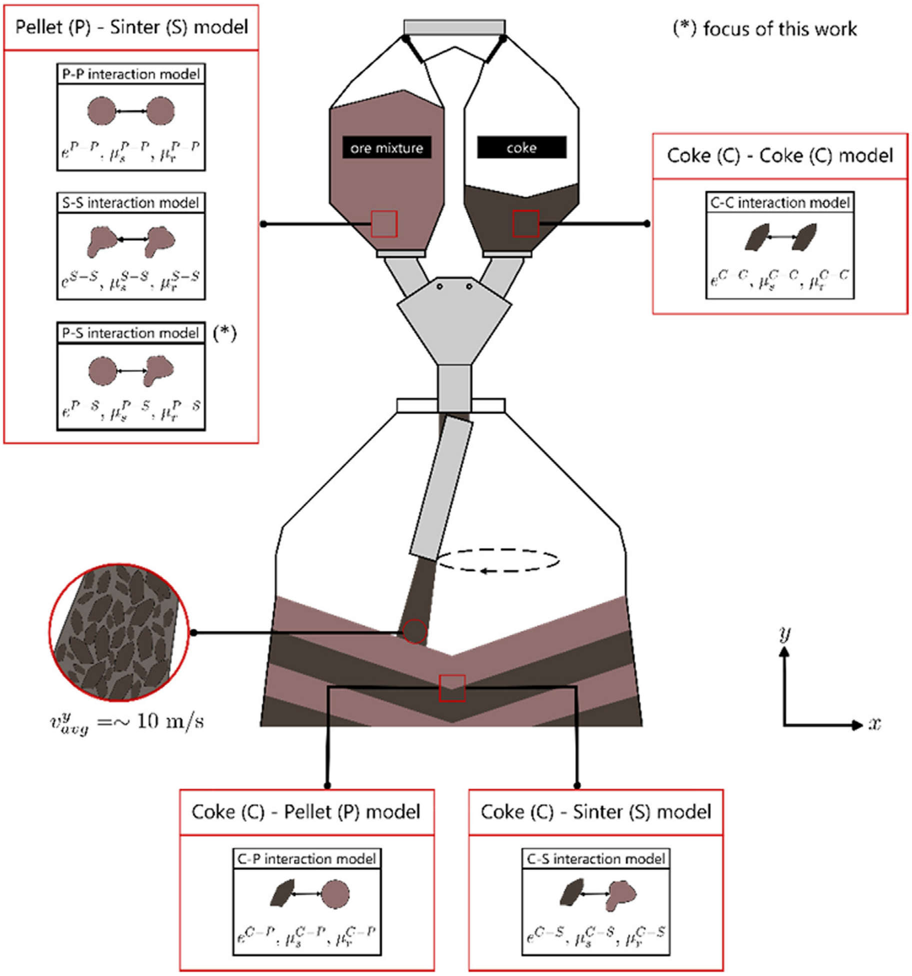

Fig. 1. Overview of required interaction parameters (restitution coefficient *e*, sliding friction coefficient μ_s, and rolling friction coefficient μ_r) for modelling blast furnace charging when using the Hertz-Mindlin contact model in combination with rolling model C in DEM simulations.

consists of a hopper which discharges material directly into a container. We investigate the effect of flow velocity by varying the discharge height, thereby scrutinizing the importance of using calibration experiments which can reproduce blast furnace flow conditions. We also use different mixture compositions, so that the results are widely applicable to blast furnace operations where ore mixture compositions may vary.

The structure of this paper is as follows. In Sec. 2, we introduce the simulation setup and methods for analysing the homogeneity and permeability in terms of the segregation index and bed porosity, respectively. In Sec. 3, we start the analysis by determining the appropriate time step and cell size, and demonstrate how segregation can be analysed in different directions. Finally, we investigate the main effects and interaction effects of the pellet-sinter interaction parameters on segregation and porosity.

The main contribution of this work is that, for the first time, it investigates the effects of interaction parameters between different components on mixture behaviour. In doing so, this work provides insight on the extent to which it is required to accurately determine pellet-sinter interaction parameters for predicting material distribution and resulting permeability of the ore layer. Hence, the results of this work can prove useful to blast furnace researchers as a first step in developing DEM models for permeability predictions and optimizations. On a higher level, the method described in this work also provides an approach for anyone who aims to determine interaction parameters for mixture models.

2. Methods

2.1. Discrete Element Method

The Discrete Element Method is used to model particulate flows by tracking the motion of each particle in the flow through numerical integration. The basic principle of DEM can be expressed as follows: if all the forces and torques acting on a particle are known at each time step of the simulation, then its trajectory can be predicted in time using Newton's second law. Given the coarse, cohesionless nature of the raw materials during furnace charging, the total force acting on a particle i is the sum of the gravitational force and interaction forces arising from the particle's contacts with surrounding objects j ($\overrightarrow{F_{ij}^c}$). The interaction force can be decomposed into a normal and tangential component ($\overrightarrow{F_{ij}^n}$ and $\overrightarrow{F_{ij}^t}$, respectively). The force and torque balance equations for particle i are thus given by [8]

$$m_i \frac{d\overrightarrow{v_i}}{dt} = m_i \overrightarrow{g} + \sum_{j=1}^{k} \left(\overrightarrow{F_{ij}^n} + \overrightarrow{F_{ij}^t} \right) \tag{1}$$

$$I_i \frac{d\overrightarrow{\omega_i}}{dt} = \sum_{j=1}^{k} \left(R_i \times \overrightarrow{F_{ij}^t} \right) + \overrightarrow{T_{ij}^r} \tag{2}$$

where $\overrightarrow{g}$ is the gravitational acceleration and m_i, R_i, v_i and ω_i are the mass, radius, velocity and angular velocity of particle i, respectively. The normal and tangential interaction forces can each be further decomposed into an elastic and dissipative component. Furthermore, the tangential interaction force is limited by the Coulomb law [22]. Hence, the interaction forces are calculated as

$$\overrightarrow{F_{ij}^n} = \left(F_{ij}^{e,n} + F_{ij}^{d,n} \right) \overrightarrow{n_{ij}} \tag{3}$$

$$\overrightarrow{F_{ij}^t} = \begin{cases} \left(F_{ij}^{e,t} + F_{ij}^{d,t} \right) \overrightarrow{t_{ij}} & \mathit{for}\ \overrightarrow{F_{ij}^t} < \mu_s \overrightarrow{F_{ij}^n} \\ \mu_s \overrightarrow{F_{ij}^n} & \mathit{otherwise} \end{cases} \tag{4}$$

where μ_s is the sliding friction coefficient between i and j.

In DEM, the particle shape is often simplified or assumed to be spherical. A fictional rolling torque (indicated by $\overrightarrow{T_{ij}^r}$ in Eq. (2) can then be applied to mimic the effect of the true particle shape in simulations. In this work, the Hertz-Mindlin no-slip model [9] is used to quantify the different force components (*cf.* Table 1) and the so-called "standard rolling model" in EDEM [10] is used to calculate the rolling torque according to

$$\overrightarrow{T_{ij}^r} = -\mu_r F_{ij}^{e,n} R^* \widehat{\omega_{ij}} \tag{5}$$

where μ_r is the rolling friction coefficient between i and j, $\widehat{\omega_{ij}}$ is the unit angular velocity vector of the object at the contact point of i and j and R^* is the effective radius, presented in Table 1.

2.2. Simulation setup

We use the software package EDEM 2022.2 on the DelftBlue high-performance cluster [23] to run simulations using the described models. The system used for this investigation consists of a hopper and a container (*cf.* Fig. 2a), with acrylic walls. The hopper outlet size is chosen such that the diameter is 10 × the diameter of the largest particle in the system and the discharge height (H) will be varied as discussed later in Sec. 2.3.2. A homogeneous mixture of pellet and sinter is created in the hopper and segregation occurs as the mixture is discharged into the container. Fig. 2b shows a snapshot of the simulation during bed formation. Using a homogeneous mixture in the hopper allows us to have a similar initial condition for each simulation run. The simulation procedure is as follows. At $t = 0$ seconds the pellet-sinter mixture is generated in the hopper by creating a volume packing with a solid fraction of 40 % in the cone-shaped volume shown in Fig. 2c. Using this method, all particles are generated at once within the cone and allowed to settle. We opt for this method rather than using a continuous particle generation with dynamic factories in order to limit segregation during hopper filling. The hopper outlet is opened at $t = 2$ seconds and the material flows into the container and is allowed to settle.

The (unscaled) particle size distributions and particle shapes for pellet and sinter, and the material properties and interaction parameters for all materials are adopted from the work of Chakrabarty et al. [24] (*cf.* Table 2) since the authors calibrated the model

Table 1
Hertz-Mindlin no-slip force models.

Parameter	Symbol	Equation	
Normal interaction force, elastic component	$F_{ij}^{e,n}$	$\frac{4}{3} E^* \sqrt{R^*} (\delta^n)^{\frac{3}{2}}$	(6)
Normal interaction force, dissipative component	$F_{ij}^{d,n}$	$-2\sqrt{\frac{5}{6}}\beta \sqrt{S^n m^*}\, v_{rel}^n$	(7)
Tangential interaction force, elastic component	$F_{ij}^{e,t}$	$-S^t \delta^t$	(8)
Tangential interaction force, dissipative component	$F_{ij}^{d,t}$	$-2\sqrt{\frac{5}{6}}\beta \sqrt{S^t m^*}\, v_{rel}^t$	(9)
Normal stiffness	S^n	$2E^* \sqrt{R^* \delta^n}$	(10)
Tangential stiffness	S^t	$8G^* \sqrt{R^* \delta^n}$	(11)
Effective radius	R^*	$\left(\frac{1}{R_i} + \frac{1}{R_j} \right)^{-1}$	(12)
Effective Young's modulus	E^*	$\left(\frac{1-\nu_i}{E_i} + \frac{1-\nu_j}{E_j} \right)^{-1}$	(13)
Effective shear modulus	G^*	$\left(\frac{2-\nu_i}{G_i} + \frac{2-\nu_j}{G_j} \right)^{-1}$	(14)
Effective mass	m^*	$\left(\frac{1}{m_i} + \frac{1}{m_j} \right)^{-1}$	(15)
Damping ratio	β	$\frac{\ln e}{\sqrt{(\ln e)^2 + \pi^2}}$	(16)

* Legend: $\delta^n =$ normal overlap, $\delta^t =$ tangential overlap, $v_{rel}^n =$ relative normal velocity, $v_{rel}^t =$ relative tangential velocity $\nu =$ Poisson ratio, $e =$ restitution coefficient.

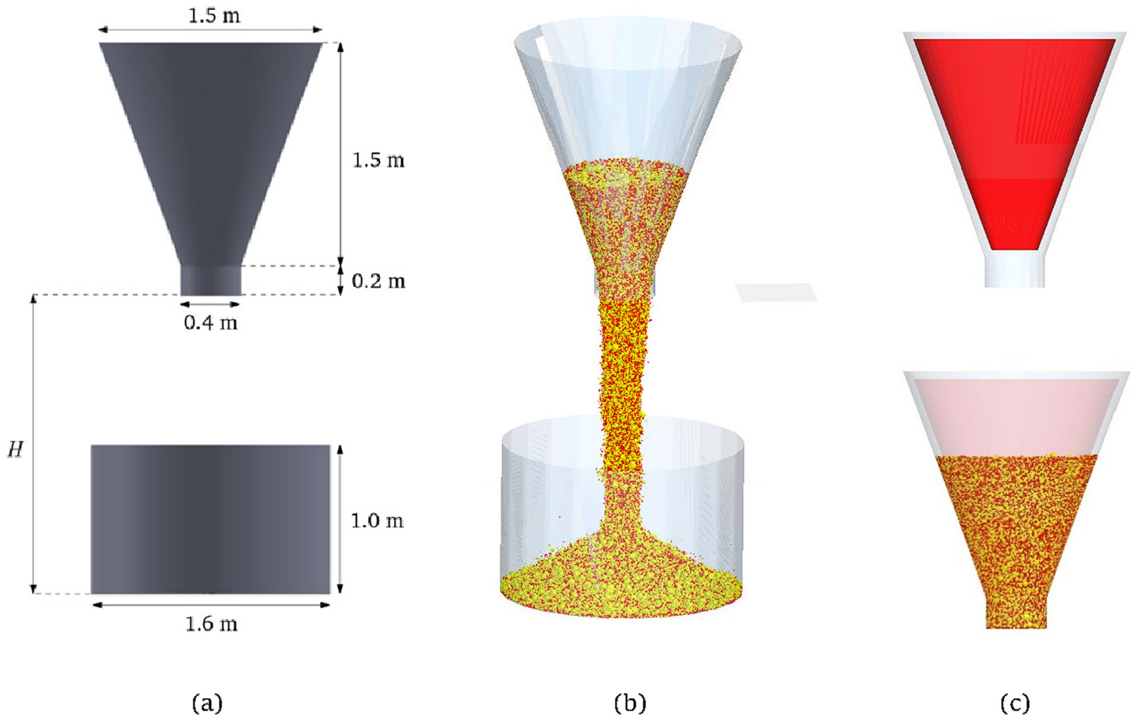

Fig. 2. (a) Simulation setup and dimensions with varying discharge height (H), (b) Demonstration of mixture discharge and bed formation in the container, (c) Cone-shaped volume used for particle generation at $t = 0$ seconds (top) and generated mixture right before opening the hopper outlet (bottom).

parameters against experimentally measured values of bulk density (2220.74 ± 27.20 kg/m^3 for pellets and 1826.67 ± 28.37 kg/m^3 for sinter) and repose angle (33.11 ± 1.56 degrees for pellets and 33.23 ± 0.27 degrees for sinter). Since pellet and sinter particles are each represented by a single shape and have multiple sizes, they can be regarded as mono-shaped, poly-sized mixtures. In their work, the authors specified the particle size ranges from Table 2; however, they did not elaborate on how the particles were generated. Our approach in this work is to specify the particle size ranges in EDEM and allow particles within each range to be generated randomly. The Euler scheme is selected for numerical integration in EDEM.

2.3. Simulation experiments

2.3.1. Time step analysis

Before executing the experiments, we determine a suitable value of the numerical time step (Δt). It is generally recommended to use a fraction of the Rayleigh time step (Δt_R), which is determined by [25]

$$\Delta t_R = \frac{\pi R\sqrt{\frac{\rho}{G}}}{0.1631\vartheta + 0.8766} \tag{17}$$

Table 2
Model parameters from Chakrabarty et al. [24]. Abbreviations: P-P = particle–particle, P-W = particle–wall.

Parameter (symbol)		Pellet	Sinter	Acrylic (wall)
Particle shapes		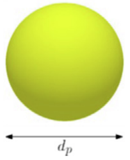 d_p	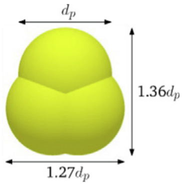 d_p $1.36d_p$ $1.27d_p$	–
Particle size (d_p) / mass percentage		6–9 mm / 5.02 % 9–12.5 mm / 68.73 % 12.5–16 mm / 26.25 %	5–10 mm / 27.97 % 10–15 mm / 28.45 % 15–20 mm / 29.91 % 20–40 mm / 13.67 %	–
Density (ρ)		3700 kg/m^3	3050 kg/m^3	1200 kg/m^3
Poisson's ratio (ϑ)		0.25	0.25	0.25
Young's modulus (E)		2.5×10^8 Pa	2.5×10^8 Pa	2.5×10^8 Pa
Restitution coefficient (e)	P-P	0.70	0.40	–
	P-W	0.70	0.40	–
Static friction coefficient (μ_s)	P-P	0.49	0.70	–
	P-W	0.38	0.38	–
Rolling friction coefficient (μ_r)	P-P	0.06	0.08	–
	P-W	0.06	0.08	–
Numerical time step Δt	to be determined (Sec. 3.1)			

where R, ρ, G and ϑ are the particle radius, particle density, shear modulus and Poisson's ratio, respectively. In EDEM, R is the value of the smallest particle size when using a range of sizes and the time step is set to 20 % of Δt_R by default [26]. According to literature, a value between 10 and 40 % of Δt_R should be used for the time step [27] and the selected value depends on the coordination number and energy in the system [26].

While the material properties are fixed, the size of the smallest particle is not necessarily the same in all simulations since particles within each size range are generated randomly. Hence, the value of Δt_R differs between simulations and is generally in the order of 3×10^{-5} s.

We consider different values of the numerical time step, ranging from 5 % to 40 % of Δt_R, and assess the effect on segregation and porosity. As the flow velocity and impact forces acting on particles during heap formation increase with the discharge height, the extreme case of $H = 6$ m will be used to determine the value of the time step. For this analysis, we use equal mass fractions of pellets and sinter in the mixture and set $e = \mu_s = \mu_r = 0.5$ for the pellet-sinter interaction parameters.

2.3.2. Effects analyses

2.3.2.1. Independent variables. The restitution coefficient, sliding friction coefficient and rolling friction coefficient between pellet and sinter are the independent variables. As seen in Table 3, each independent variable has three test levels, resulting in 27 simulations for a full factorial design. Additionally, each simulation is repeated three times to account for the stochastic nature of the flow.

2.3.2.2. Dependent variables. The segregation index and bed porosity are the response variables for our investigation. First, the positions and volumes of pellet and sinter particles are extracted from EDEM at the end of each simulation. These data are then imported to Matlab for segregation and porosity analyses.

2.3.2.2.1. Component segregation. Segregation in a granular system can be quantified using a segregation index. There are generally two approaches for calculating a segregation index in literature [28]: sampling-based and non-sampling methods. In the sampling-based approach, the system of particles is divided into a number of sub-domains (samples), and the concentration of one particle type (called the "tracer") in the mixture is determined in each sample. A statistical approach is then taken to measure the difference of tracer particle concentration between the samples and the segregation index is a measure for this deviation. The main advantage of using a sampling-based segregation index is that it is significantly faster to compute than a non-sampling based index. In this work, pellets are the tracer particles and the mass fraction of pellets (x_P) is determined for each sub-domain. The segregation index is then defined as the relative standard deviation of x_P [29]

$$SI = \sqrt{\frac{\sum_{i=1}^{N}\left(x_P^i - \bar{x}_P\right)^2}{N-1}} \tag{18}$$

where N is the number of sub-domains, $\bar{x}_P$ is the average mass fraction of all domains, determined by

Table 3
Factors and levels tested. Abbreviation: P-S = pellet-sinter.

Independent variable (unit)	Low level	Intermediate level	High level
e^{P-S}(-)	0.1	0.5	0.9
μ_s^{P-S}(-)	0.1	0.5	0.9
μ_r^{P-S}(-)	0.1	0.5	0.9

$$\bar{x}_P = \frac{x_P^1 + \cdots + x_P^N}{N} \tag{19}$$

and x_P^i is the mass fraction of pellets in the i-th cell determined by

$$x_P^i = \frac{m_P^i}{\left(m_P^i + m_S^i\right)} \tag{20}$$

where m_P^i and m_S^i are the mass of pellet and sinter particles in bin i, respectively. The value of SI ranges from 0.0 to 1.0, where 0.0 represents a perfectly mixed state and 1.0 represents a fully segregated state.

In order to analyse segregation in different directions, we consider three domain decomposition techniques: radial, vertical and circumferential. Fig. 3 illustrates how equal-volume subdomains are defined for radial, vertical and circumferential directions, and how the subdomains are numbered for reference in Sec. 3.

Despite fast computation times, it is well known that the value of a sampling-based segregation index depends on the size (and hence number) of the sub-domains used for its calculation [30]. As this work is concerned with investigating the effects of interaction parameters on the segregation value, it is important to understand whether the sample size affects our interpretation of the effects in different directions. Hence, we will also investigate how sensitive the relationships between independent variables and the segregation index are to the sample size.

2.3.2.2.2. Porosity. The permeability of a packed bed provides a measure for how well the voids between particles comprising the bed (*i.e.*, the pores) are connected. Hence, the permeability gives an indication of the ease with which a fluid can flow through the bed. It is generally determined by measuring flow characteristics such as the pressure drop across the bed, rather than properties of the bed itself. Since this work does not consider fluid-particle interaction, we use the bed porosity as an indicator of the permeability. Although the permeability does not depend on the porosity alone but also on how the well the pores are connected, it is reasonable to assume that a high porosity is indicative of high permeability, and vice versa [31]. The porosity (P) is defined as the volume fraction of pores in the bed and can directly be calculated as

$$P = \frac{V_b - V_p}{V_b} \tag{21}$$

where V_p is the total volume of all particles in the bed and V_b is the bed volume. The value of V_p is easily determined in DEM and the value of V_b is approximated by using alphaShape in Matlab, which creates a bounding volume for a set of 3-D points (in this case the x, y and z coordinates of all particles).

2.3.2.3. Control variables. As we stated in [7], the vertical flow velocity upon striking the stock surface in a blast furnace is in the order of 10 m/s. Nonetheless, blast furnace model calibration is generally done using low-velocity experiments. It is currently unclear how important the flow velocity is with respect to the calibration outcome, *i.e.*, how the calibrated values of model parameters change when using different flow velocities. Similarly, it is not yet understood how the calibrated values of mixture interaction parameters change for different mixture compositions. This is important to understand since the composition is an operational parameter which can be tuned to improve furnace performance in practise. As a first step, we investigate to which degree the flow velocity and mixture composition affect the sensitivity of SI and P to e^{P-S}, μ_s^{P-S} and μ_r^{P-S}.

The flow velocity during bed formation is varied by using different values of the discharge height H and the composition is varied by adjusting the mass fractions of pellets in the mixture (x_P) which

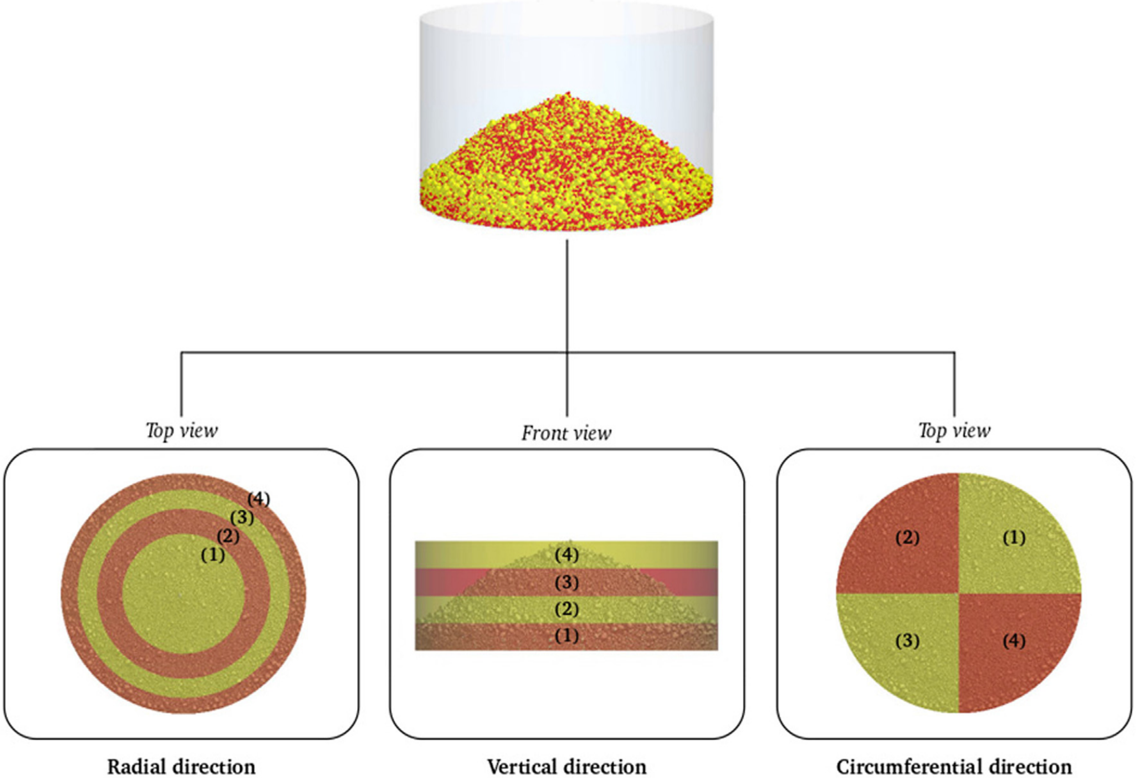

Fig. 3. Illustration of equal-volume samples in radial, vertical and circumferential directions.

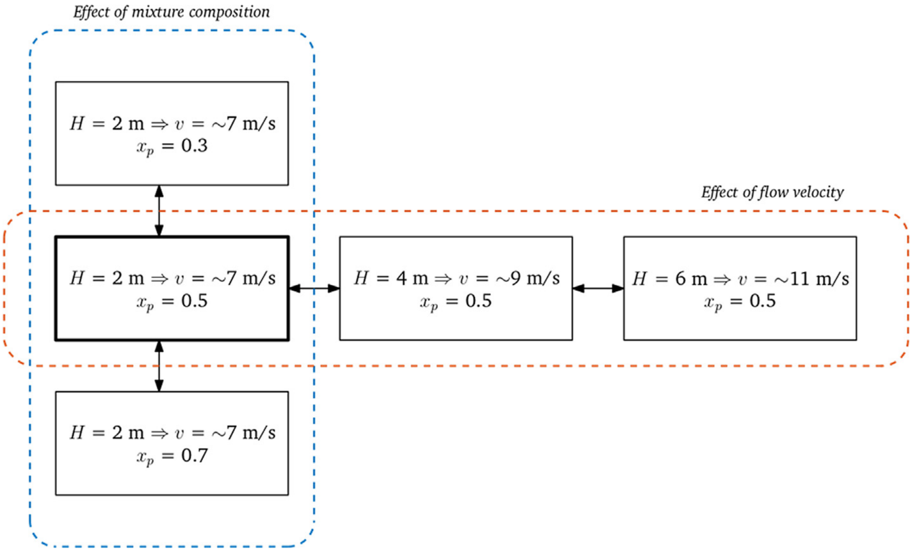

Fig. 4. Overview of the different cases for which the effects of e^{P-S}, μ_s^{P-S} *and* μ_r^{P-S} on *SI* and *P* are investigated.

is generated inside the cone-shaped volume of Fig. 2. We define a reference case where $H = 2$ meters and $x_P = 0.5$, and perform the full factorial design for different cases to take into account the effects of the flow velocity and the mixture composition, as shown in Fig. 4.

3. Results and discussion

3.1. Time step determination

Since this work is concerned with analysing segregation and porosity, we first investigate how the time step Δt affects these parameters. Fig. 5a shows the results of the segregation analysis using 4 domains in radial, vertical and circumferential directions. It can be seen that there is practically no effect of the time step on segregation in circumferential direction. This result is to be expected due to the symmetrical nature of the discharging process in circumferential direction. In vertical direction, the predicted segregation increases significantly when $\Delta t > 0.1 \times \Delta t_R$ while the segregation decreases slightly after this point in radial direction. Based on these results, a time step of $0.1 \times \Delta t_R$ appears to be suitable. However, Fig. 5b shows that the predicted bed porosity decreases almost linearly with increasing value of the time step, so that the choice of the time step with respect to the porosity is not straightforward.

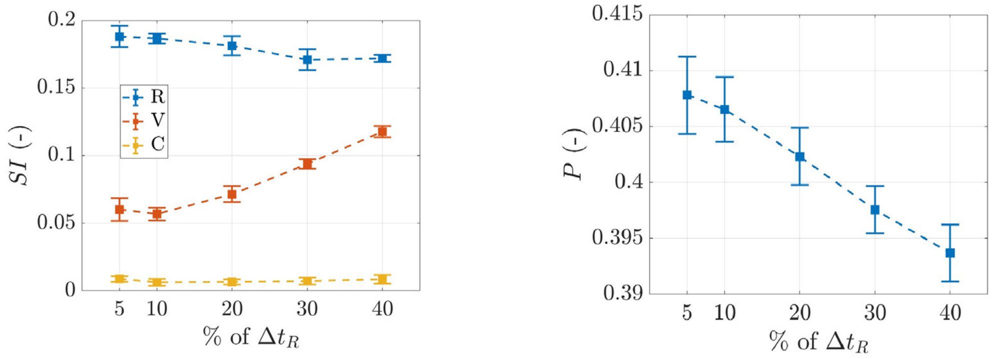

(a) (b)

Fig. 5. Effect of the time step on (a) segregation in radial (R), vertical (V) and circumferential (C) directions and (b) overall bed porosity. Error bars indicate the standard deviation of the pellet mass fraction based on six repetitions.

We further investigate the effect of the time step on a sub-domain level by considering the component and porosity distributions in radial and vertical directions, as shown in Fig. 6 and Fig. 7, respectively. From Fig. 5 it is clear that the mass fraction distribution of pellets and porosity distribution in radial direction are unaffected by the time step until $0.1 \times \Delta t_R$. Although this is not so obvious in vertical direction, it can still be observed that the predicted mass fraction distribution changes significantly when $\Delta t > 0.1 \times \Delta t_R$, especially in the bottom layer of the heap. Hence, we conclude that $\Delta t = 0.1 \times \Delta t_R$ is indeed suitable for this work.

3.2. Individual factor effects

In this section, we show how segregation in radial, vertical and circumferential directions and porosity depend on pellet-sinter sliding friction, rolling friction and restitution coefficient under different operational conditions and for different mixture compositions. The results are presented in main effect plots, which allow us to compare the relative strength of the independent variables on the dependent variables [32].

3.2.1. Effect of sample size on segregation index

Fig. 8a-c show the main effect plots for e^{P-S}, μ_s^{P-S} and μ_r^{P-S} for the reference case using different sample sizes. Each figure shows the plots in radial, vertical and circumferential directions for the reference case. It is clear that the values of SI in radial and circumferential directions are unaffected by the number of samples, while the value in vertical direction decreases as the number of samples increases. Also, when using 3 samples, the plot trends for vertical segregation are slightly different compared to trends when using 4 or 5 samples. For example, vertical segregation increases with e^{P-S} for high values of e^{P-S} (> 0.5) when using 3 layers, while the opposite effect is seen when using 4 or 5 layers. For the sliding friction coefficient, the plot is almost perfectly horizontal when using 3 layers, while this is not the case when using 4 or 5 layers. For the rolling friction coefficient, a relatively strong effect on vertical segregation in observed for low values of μ_r^{P-S} (< 0.5) when using 3 layers, while very little effect is seen for that range when using 4 or 5 layers. These observations also hold for other discharge heights and mixture compositions, as shown in Appendix A. Hence, we conclude that using 3 layers in vertical direction is insufficient for our analyses and 4 sub-domains are used in both vertical and radial directions in the remainder of this work.

We also consider a case where the bed is divided into sub-domains in multiple directions. We will use the term “combined segregation index (SI_c)” throughout this work to refer to the segregation index when determined in this way. As shown in Sec. 3.1 and according to Fig. 8, segregation in circumferential direction is negligible compared to the other two directions. Therefore, we divide the bed into both radial and vertical directions (using an equal numbers of rings and layers) and calculate SI_c using Eq. (18). Fig. 9 shows the results for the reference case. It can be seen that there is an effect of the sample size in all cases. The most important observation is that the effects of e^{P-S} and μ_r^{P-S} when

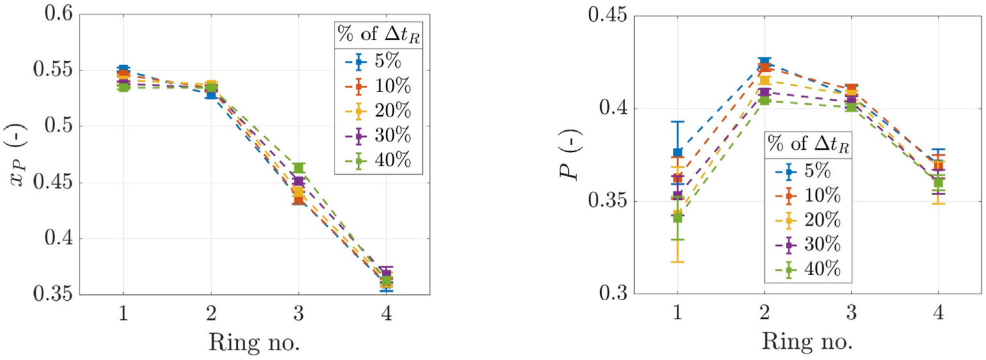

(a) (b)

Fig. 6. Effect of the time step on (a) the mass fraction distribution of pellets and (b) the porosity distribution in radial direction. Error bars indicate the standard deviation of the pellet mass fraction based on six repetitions.

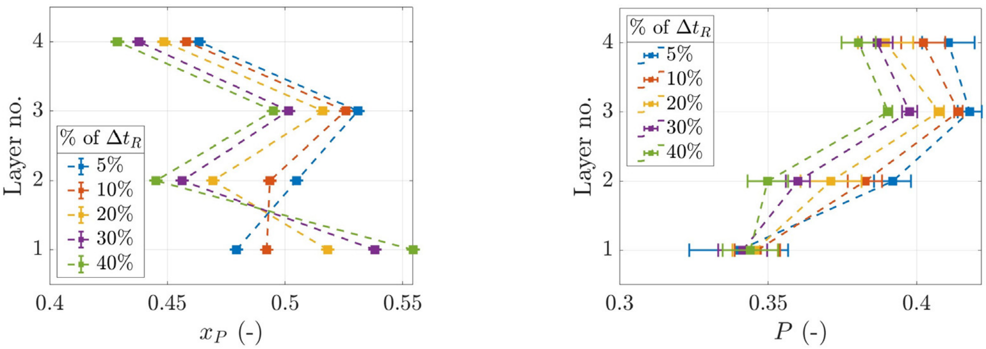

(a)

(b)

Fig. 7. Effect of the time step on (a) the mass fraction distribution of pellets and (b) the porosity distribution in vertical direction. Error bars indicate the standard deviation of the pellet mass fraction based on six repetitions.

using the smallest sample size (3 rings and 3 layers) are opposite to the effects observed for larger sample sizes. However, it can also be seen that the SI_c error bars are relatively large when compared to SI error bars in individual radial, vertical and circumferential directions (*cf.* Fig. 8). This makes it impossible to confidently interpret the effect plots in Fig. 9. Since the error bars represent the standard deviation, further research is required to scrutinise the number of repetitions which allows the SI_c plots to be interpreted. For the remainder of this work, we will focus on investigating the segregation in radial and vertical directions separately.

3.2.2. Reference case

As a first step, we present the effect plots for the reference case, in which $H = 2$ meters and $x_P = 0.5$.

3.2.2.1. Segregation. Fig. 10 shows the main effect plots for e^{P-S}, μ_s^{P-S} and μ_r^{P-S} on segregation in radial, vertical and circumferential directions. Based on the SI values, it is clear that the degree of segregation is most significant in radial direction and least significant in circumferential direction. The latter is to be expected since particles primarily move in vertical direction during hopper discharge and subsequently spread out radially as the container is filled. Moreover, Fig. 10c shows that the interaction parameters do not affect segregation in circumferential direction as the plots are horizontal. Fig. 10a and b show an effect of all three parameters on radial and vertical segregation, although the effects are much stronger in radial direction.

While the value of the segregation index gives an indication of how well the components are mixed in the container, it does not provide insight on where the different components are concentrated in case of uneven distribution. This makes it difficult to interpret the effects of the interaction parameters based on Fig. 10a–c. Therefore, in Fig. 11– Fig. 13, we provide a better understanding of how pellet and sinter particles are distributed for different values of e^{P-S}, μ_s^{P-S} and μ_r^{P-S} using distribution plots.

From Fig. 11 it is clear that pellets are mostly concentrated at the centre of the heap (ring 1 and 2) and the concentration rapidly decreases towards the container wall. It can be seen that the distribution of pellets tends to become more homogeneous for increasing and decreasing values of restitution and friction coefficients, respectively. In vertical direction, Fig. 12 shows that there is a higher concentration of pellets at the bottom layers of the bed when μ_s^{P-S} and μ_r^{P-S} are low. This indicates that low friction values allow for easier percolation of pellets towards the bottom of the bed. Fig. 13 shows that pellets are distributed homogeneously in circumferential direction, regardless of the values of the interaction parameters. Moreover, $x_P \approx 0.5$ in all cases so that, by definition of Eq. (13), $SI \approx 0$ as seen in Fig. 10**c.** Hence, we will neglect the circumferential segregation in the remainder of this work.

3.2.2.2. Porosity. Fig. 14 shows that there is a clear effect of all three interaction parameters on the bed porosity. The porosity increases, indicating that the bed has larger voids, for higher values of the pellet-sinter sliding and rolling friction coefficients. The opposite relationship can be observed for the pellets-sinter restitution coefficient: the porosity tends to increase for lower values of the restitution coefficient. To get a better understanding of these effects, we look into the particle contacts during hopper discharge. Fig. 15a-c show the effects of e^{P-S}, μ_s^{P-S} and μ_r^{P-S}, respectively, on the number fraction of pellet-pellet, sinter-sinter and pellet-sinter contacts. In each plot, the value of one parameters is varied from 0.1 to 0.9 while the values for the other two interaction parameters were kept at 0.5. Fig. 15b and c show that the number of pellet-sinter contacts is higher for high values of μ_s^{P-S} and μ_r^{P-S}. This can possibly be explained by the fact that high friction increases the contact resistance between pellet and sinter, thereby impeding their relative motion as they come into contact. As a result, the number of pellet and sinter particles which are in contact in the stable heap are higher than for low values of μ_s^{P-S} and μ_r^{P-S}. Fig. 15a shows that the number of pellet-sinter contacts is lower for high values of e^{P-S}, which can be explained by the fact that pellet and sinter particles have high mobility and therefore move away from each other after colliding when e^{P-S} is high. Based on these results, there appears to be a relationship between the component distribution and the overall bed porosity.

3.2.3. Effect of flow velocity

Fig. 16 and Fig. 17 show the main effect plots for e^{P-S}, μ_s^{P-S} and μ_r^{P-S} on segregation and porosity, respectively, for $x_p = 0.5$ when using different discharge heights. First and foremost, Fig. 16a-c show clear effects of e^{P-S}, μ_s^{P-S} and μ_r^{P-S} on either radial or vertical segregation, or both, for all discharge heights. According to Fig. 17, this also holds for the porosity. Hence, all three interaction parameters must be calibrated for predicting component segregation and bed permeability, regardless of the flow velocity.

Looking more closely, the flow velocity does not seem to affect the plot trends when it comes to the porosity, since the plots in Fig. 17 are nearly parallel for all three parameters. This also holds for segregation in radial direction, while it is not the case for segregation in vertical direction. Fig. 16b and c show that the effects

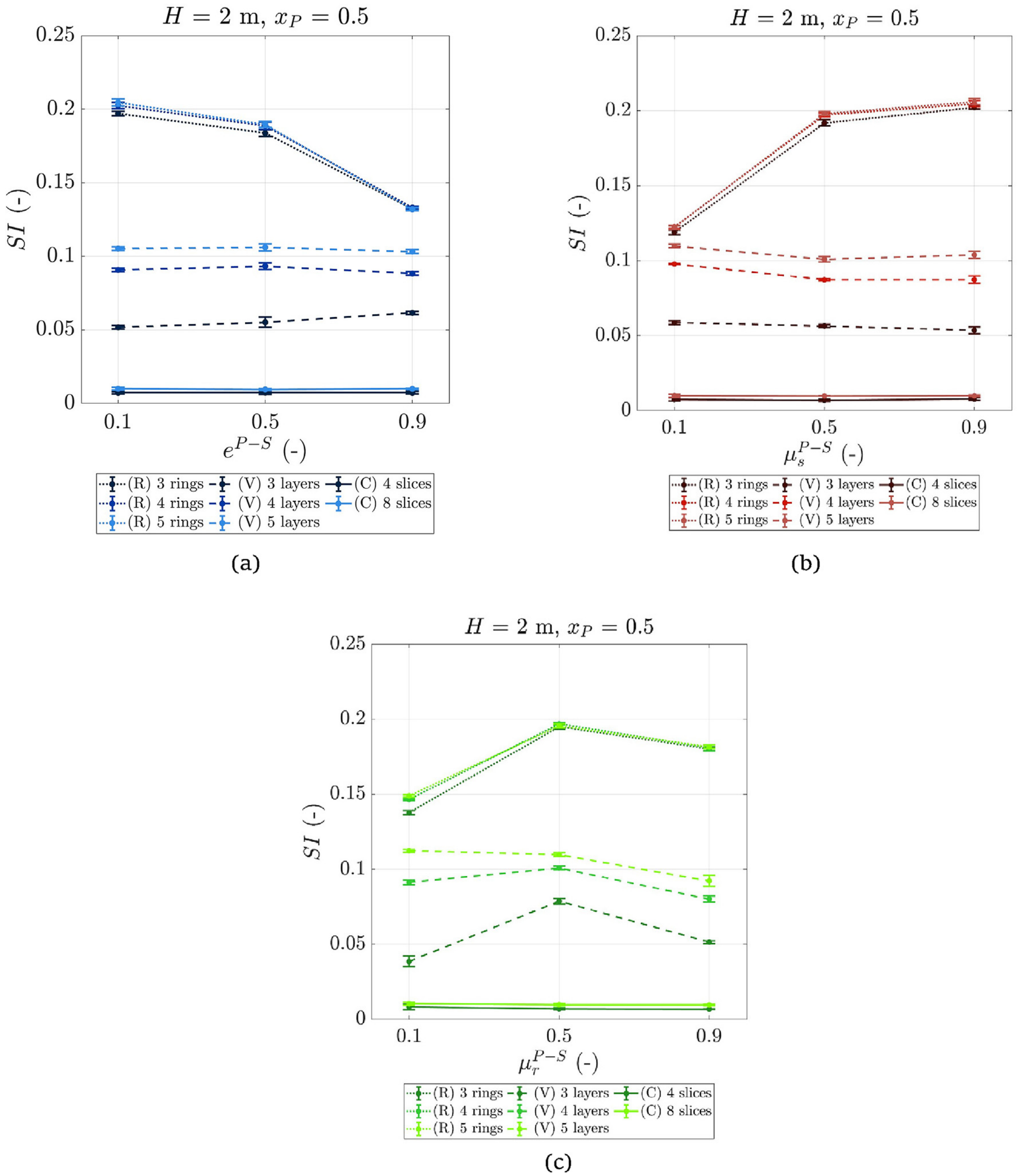

(a)

(b)

(c)

Fig. 8. Effects of (a) e^{P-S}, (b) μ_s^{P-S} and (c) μ_r^{P-S} on segregation in radial (R) and vertical (V) and circumferential (c) directions for $H = 2$ m and $x_P = 0.5$ calculated using different sample sizes. Error bars indicate the standard deviation of the segregation index based on three repetitions.

of μ_s^{P-S} and μ_r^{P-S} on vertical segregation change at larger discharge heights. Besides the fact that the effects of μ_s^{P-S} and μ_r^{P-S} are relatively weak for $H = 2$ m, it is clear that vertical segregation increases for $0.1 < \mu_r^{P-S} < 0.5$ when $H = 2$ m, while the opposite effect is seen for $H = 4$ meters and $H = 6$ meters. Hence, the nature of the effect of μ_r^{P-S} on vertical segregation seems to depend on the flow velocity. Another observation is that segregation in radial direction is reduced with increasing discharge height, while segregation in vertical direction increases with the discharge height. In all cases, the effect plots for $H = 4$ meters and $H = 6$ meters are similar in both trends and values, suggesting that there exists a velocity threshold beyond which there is no significant effect on vertical segregation.

3.2.4. Effect of mixture composition

Fig. 18 and Fig. 19 show the effects of e^{P-S}, μ_s^{P-S} and μ_r^{P-S} on segregation and porosity, respectively, for $H = 2$ meters when using different mixture compositions. Fig. 19 shows that the porosity decreases with lower mass fraction (*i.e.*, more sinter particles) of pellets. Considering the particle shape, this result is expected since it is well known from literature that non-spherical particles generally produce a higher packing density (*i.e.*, lower porosity) than spherical particles with equivalent size distributions [33,34]. Besides the particle shape, it must be noted that the pellet and sinter particles in this work have different size distributions (*cf.* Table 2), and the amount of sinter fines (5–10 mm / 27.97 %) is significantly higher than the amount of pellet fines (6–9 mm / 5.02 %).

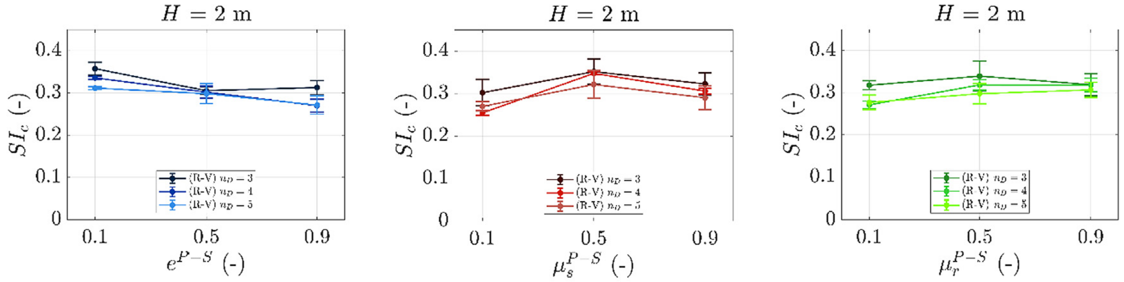

(a) (b) (c)

Fig. 9. Effects of (a) e^{P-S}, (b) μ_s^{P-S} and (c) μ_r^{P-S} on segregation in combined radial and vertical directions calculated using different sample sizes. Error bars indicate the standard deviation of the combined segregation index based on three repetitions.

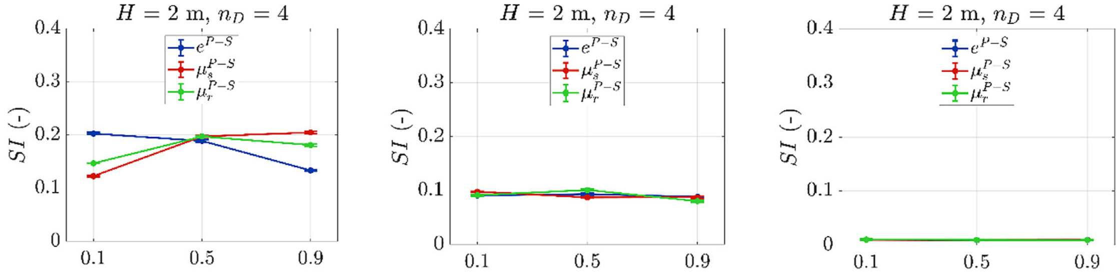

(a) (b) (c)

Fig. 10. Effect of pellet-sinter interaction parameters on segregation in (a) radial, (b) vertical and (c) circumferential directions.

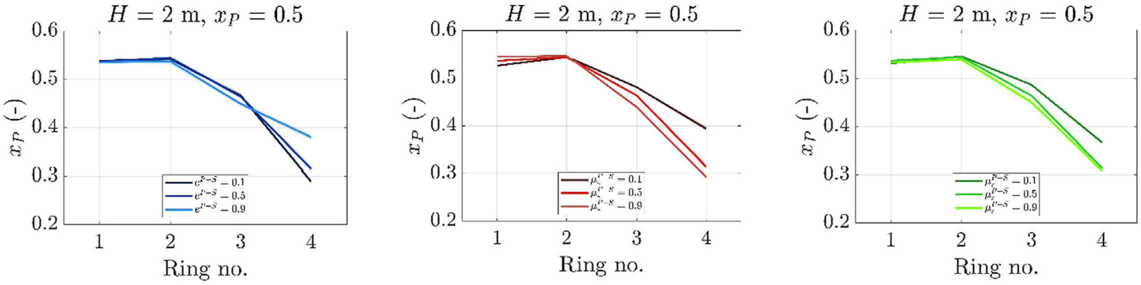

(a) (b) (c)

Fig. 11. Effect of (a) e^{P-S}, (b) μ_s^{P-S} and (c) μ_r^{P-S} on the pellet distribution in radial direction. Shaded areas indicate the standard deviation of the pellet mass fraction based on three repetitions.

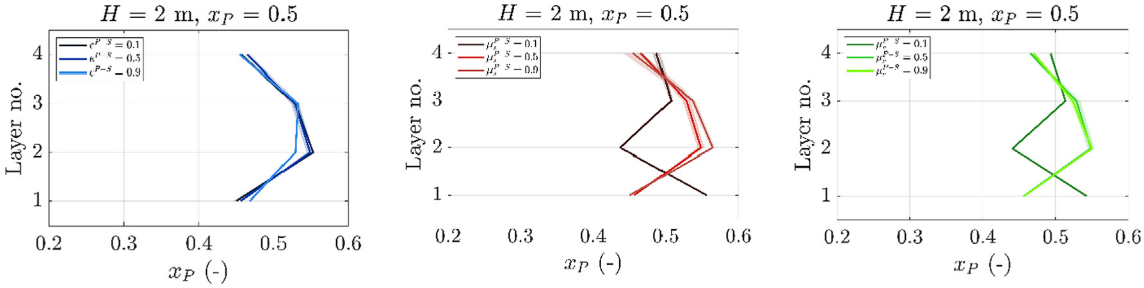

(a) (b) (c)

Fig. 12. Effect of (a) e^{P-S}, (b) μ_s^{P-S} and (c) μ_r^{P-S} on the pellet distribution in vertical direction. Shaded areas indicate the standard deviation of the pellet mass fraction based on three repetitions.

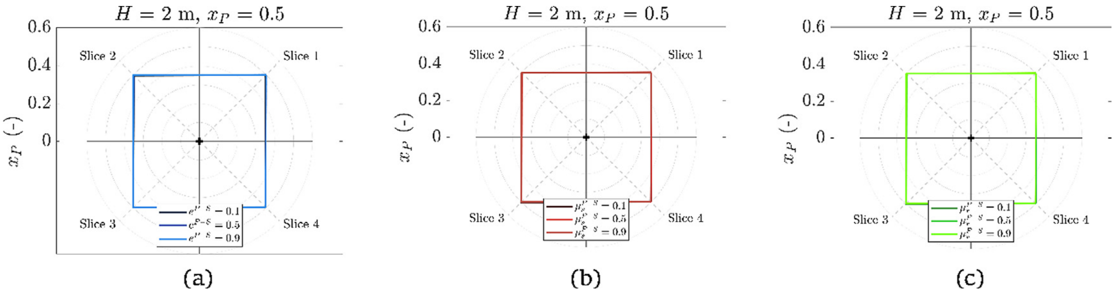

(a) (b) (c)

Fig. 13. Effect of (a) e^{P-S}, (b) μ_s^{P-S} and (c) μ_r^{P-S} on the pellet distribution in circumferential direction. Shaded areas indicate the standard deviation of the pellet mass fraction based on three repetitions.

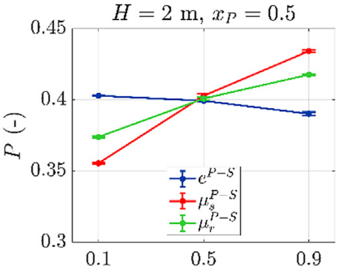

Fig. 14. Effect of pellet-sinter interaction parameters on heap porosity.

The fines ratio is also expected to contribute to the high packing density of sinter.

Based on the segregation values in Fig. 18, it can be concluded that the degree of segregation increases with lower mass fraction of pellets in the mixture in radial direction, while the segregation in vertical direction is highest when $x_P = 0.5$. We also conclude that the mixture composition does not affect the trends in radial direction since we observe similar effects on radial segregation for the different compositions. The effects in vertical direction are much weaker than in radial direction and different effects of μ_s^{P-S} and μ_r^{P-S} are seen depending on the composition: similar trends are seen when $x_P = 0.5$ and $x_P = 0.7$, while an opposite trend is seen for $x_P = 0.3$. Also, the friction coefficients seem to have stronger effects on vertical segregation when $x_P = 0.3$. For the restitution coefficient, the *SI* value increases very slightly as e^{P-S} increases from 0.5 to 0.9 when $x_P = 0.3$ and $x_P = 0.7$, while an opposite trend is seen for $x_P = 0.5$. However, since this difference is barely visible, it can be said that the mixture composition has a weaker effect on the e^{P-S} trends when compared to the μ_s^{P-S} and μ_r^{P-S} trends. Regardless of the trends, it is clear that e^{P-S}, μ_s^{P-S} and μ_r^{P-S} must be calibrated for predicting component segregation and bed permeability regardless of the mixture composition due to their clear effects on radial segregation and porosity.

3.3. Interaction effects

In this section we use interaction plots to present how pellet-sinter sliding friction, rolling friction and restitution coefficient mutually affect segregation in radial, vertical and circumferential directions and porosity. An interaction plot between two independent variables is constructed by showing the levels of one independent variable on the *x*-axis and the dependent variable on the *y*-axis, and plotting separate lines for each level of the second independent variable. If the individual lines are parallel, then there is no interaction between the two independent variables. If, however, the lines have different slopes or intersect, then there is some interaction and the interaction is stronger with increasing slope difference.

In our previous work [7], we summarized which studies in literature have reported pellet-sinter interaction parameters. By considering the reported values of e^{P-S}, μ_s^{P-S} and μ_r^{P-S} from these works, we have indicated which regions of the plots are likely to be applicable to pellet-sinter interactions using dashed boxes. Thicker dashed lines are used to indicate when interactions are significant based on differences in slopes. For clarity, we present only the plots corresponding to the reference case here and refer to the appendices for additional plots relating to other cases.

Fig. 20 and Fig. 21 show the interaction plots for the reference case in radial and vertical segregation index, respectively. In radial direction, only the interaction between μ_s^{P-S} and μ_r^{P-S} is noteworthy for $\mu_s^{P-S} > 0.5$. In vertical direction, the interaction between μ_s^{P-S} and μ_r^{P-S} is also relevant for $\mu_r^{P-S} < 0.5$. For radial segregation, the results for $H = 4$ meters and $H = 6$ meters (*cf.* Fig. B1 and B2 in

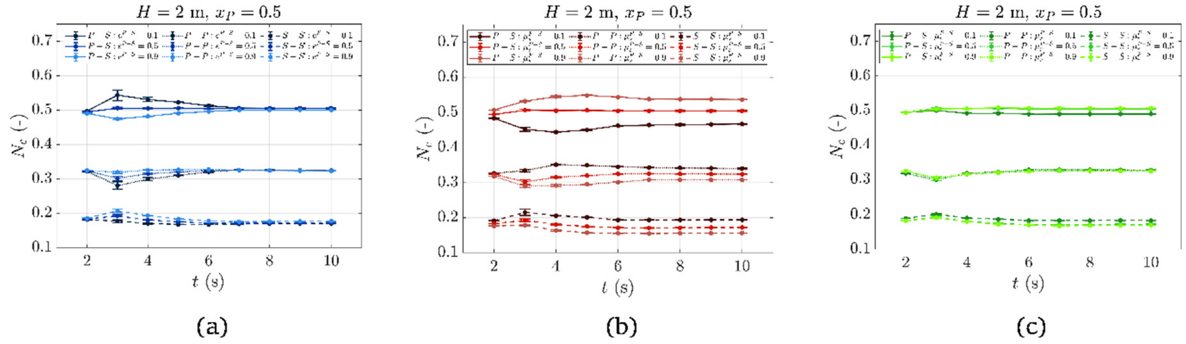

(a) (b) (c)

Fig. 15. Effect of (a) e^{P-S}, (b) μ_s^{P-S} and (c) μ_r^{P-S} on the fraction of pellet-pellet (P-P), sinter-sinter (S-S) and pellet-sinter (P-S) contacts during hopper discharge.

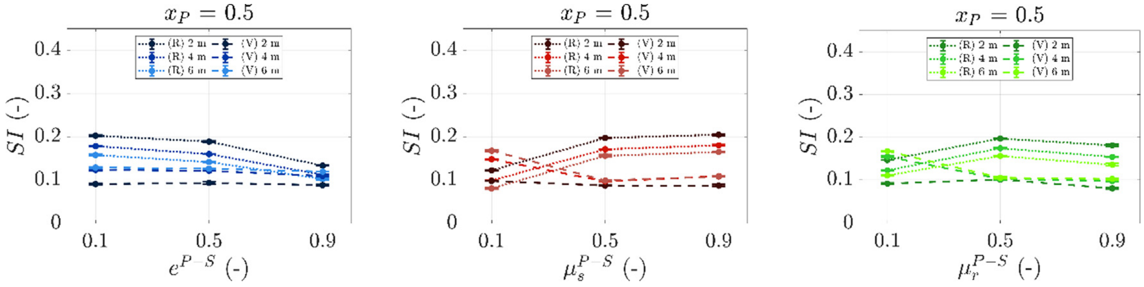

(a) (b) (c)

Fig. 16. Effects of (a) e^{P-S}, (b) μ_s^{P-S} and (c) μ_r^{P-S} on segregation in radial (R) and vertical (V) directions for different discharge heights. Error bars indicate the standard deviation of the segregation index based on three repetitions.

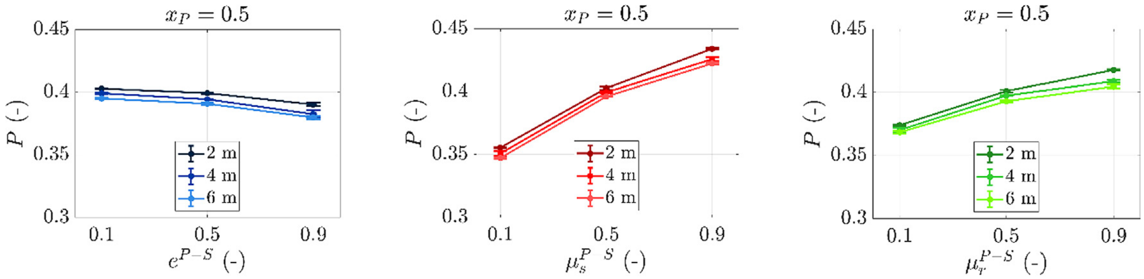

(a) (b) (c)

Fig. 17. Effects of (a) e^{P-S}, (b) μ_s^{P-S} and (c) μ_r^{P-S} on the overall porosity for different discharge heights. Error bars indicate the standard deviation of the segregation index based on three repetitions.

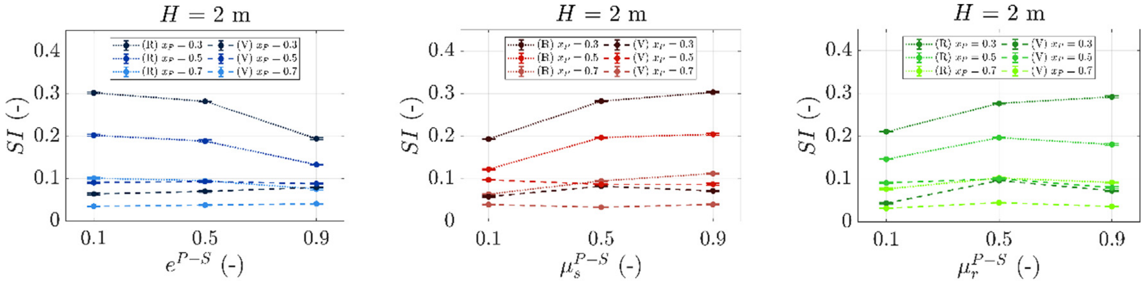

(a) (b) (c)

Fig. 18. Effects of (a) e^{P-S}, (b) μ_s^{P-S} and (c) μ_r^{P-S} on segregation in radial (R) and vertical (V) directions for different mixture compositions. Error bars indicate the standard deviation of the segregation index based on three repetitions.

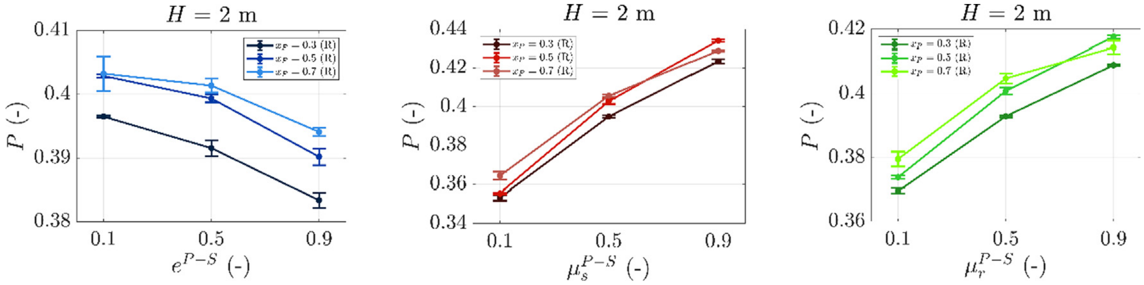

(a) (b) (c)

Fig. 19. Effects of (a) e^{P-S}, (b) μ_s^{P-S} and (c) μ_r^{P-S} on the overall porosity for different mixture compositions. Error bars indicate the standard deviation of the segregation index based on three repetitions.

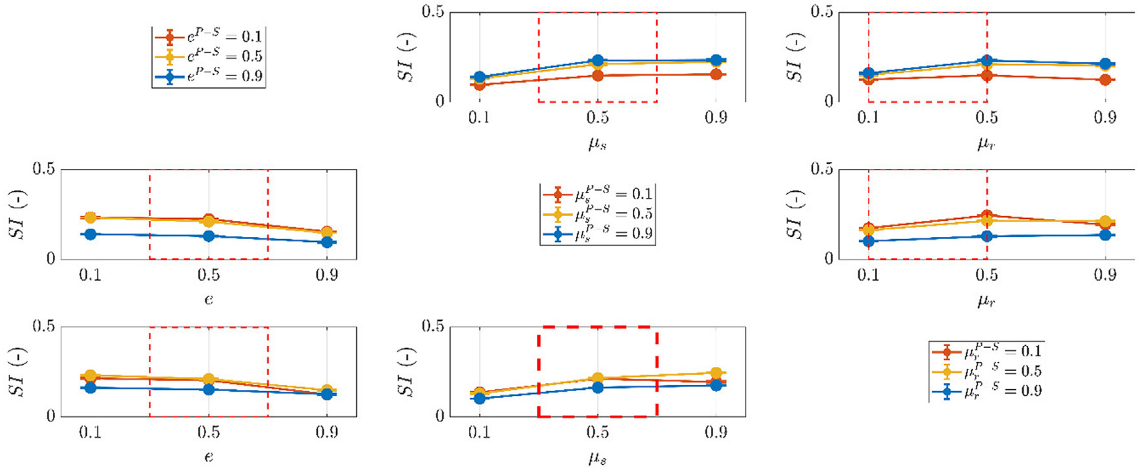

Fig. 20. Interaction effects of e^{P-S}, μ_s^{P-S} and μ_r^{P-S} on radial segregation for the reference case. Error bars indicate the standard deviation of the segregation index based on three repetitions. (Thick) dashed boxes indicate (important) regions of interest.

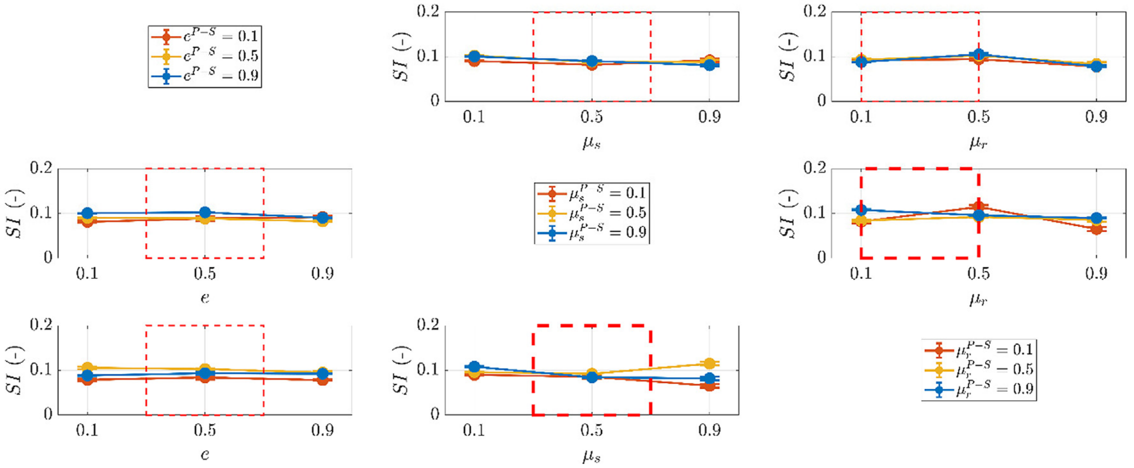

Fig. 21. Interaction effects of e^{P-S}, μ_s^{P-S} and μ_r^{P-S} on vertical segregation for the reference case. Error bars indicate the standard deviation of the segregation index based on three repetitions. (Thick) dashed boxes indicate (important) regions of interest.

Appendix B) are very similar to the reference case with significant interaction between μ_s^{P-S} and μ_r^{P-S} for $\mu_s^{P-S} > 0.5$. This also holds for vertical segregation (*cf.* Fig. B3 and Fig. B4); however, the interactions are between μ_s^{P-S} and μ_r^{P-S} are stronger compared to the reference case. The interaction plots for $x_P = 0.3$ and $x_P = 0.7$ in radial direction are presented in Fig. B7 and Fig. B8, respectively. Similar to the reference case, interactions between μ_s^{P-S} and μ_r^{P-S} for $\mu_s^{P-S} > 0.5$ can be seen for $x_P = 0.7$. Interestingly, no interaction is observed for $x_P = 0.3$. In vertical direction (*cf.* Fig. B9 and Fig. B10) there are interactions between μ_s^{P-S} and μ_r^{P-S}, similar to the reference case.

Fig. 22 shows the interaction plots for the porosity in the reference case. Similar to the segregation index, we observe weak interactions between μ_s^{P-S} and μ_r^{P-S}. This also holds for other discharge heights (*cf.* Fig. B5 and Fig. B6) and mixtures compositions (*cf.* Fig. B11 and Fig. B12).

In Sec. 3.2 we already concluded that e^{P-S}, μ_s^{P-S} and μ_r^{P-S} should each be carefully calibrated when developing a model for predicting segregation. The results in this section show that, for all investigated mixture compositions and flow velocities, the effects of μ_s^{P-S} and μ_r^{P-S} on segregation and porosity are dependent on each other. This means that that once a model has been calibrated, these parameters cannot be changed independently. It is sometimes seen in literature that researchers adopt model parameters from other publications regardless of the particle shapes used; for example, Yu & Saxén [35] modelled coke as non-spherical particles and used the sliding friction coefficient from the work of Mio et al. [36], where coke particles were modelled as spheres. By using different shapes, the particle rolling behaviour is different and, based on our findings, the effect of sliding friction on segregation and porosity will also be altered. It is therefore recommended to either use models exactly as they are presented in literature, or re-calibrate them when adjusting the frictional behaviour.

4. Conclusions

In this work, we identified the importance of pellet-sinter interaction parameters on the homogeneity (segregation) and permeability (porosity) of a bed created through hopper discharge. The effect of pellet-sinter interaction parameters on the bed formation

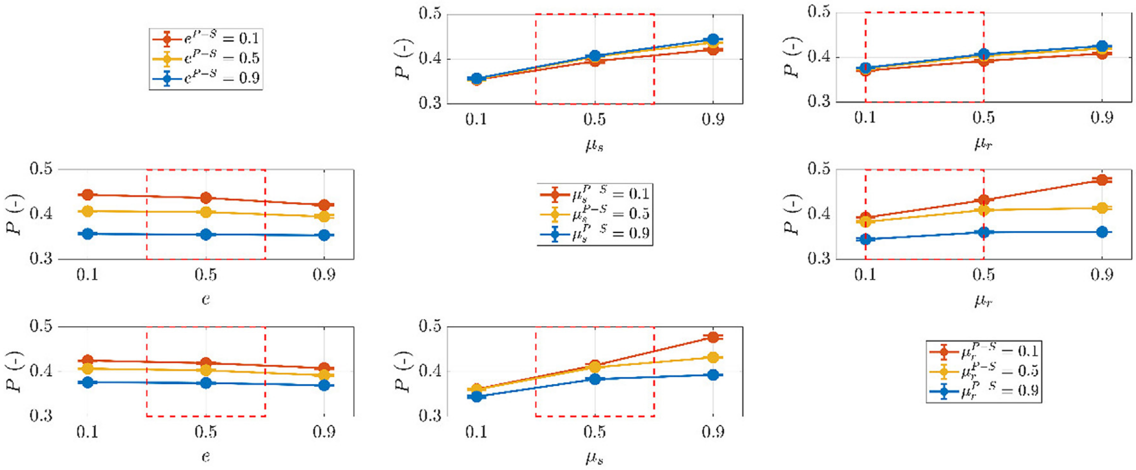

Fig. 22. Interaction effects of e^{P-S}, μ_s^{P-S} and μ_r^{P-S} on porosity for the reference case. Error bars indicate the standard deviation of the segregation index based on three repetitions. Dashed boxes indicate regions of interest.

was investigated using a range of values for the interaction parameters, different mixture compositions and under different flow velocities. The conclusions of this work are as follows:

- All three interaction parameters have clear independent effects on both segregation and porosity, regardless of the mixture composition and flow velocity. Therefore, each of these parameters must be carefully calibrated when developing a DEM model to predict the permeability of an ore layer charged to a blast furnace.
- It is often more difficult to interpret effect plots using a combined segregation index rather than individual segregation indices for radial, vertical and circumferential directions due to relatively large uncertainties. Analysing segregation separately in each direction is therefore more convenient. We found that the pellet-sinter restitution coefficient reduces radial segregation while the opposite is true for the friction coefficients, regardless of the flow velocity and mixture composition used. In vertical direction, there is barely an effect of restitution coefficient while the effect of friction coefficients depends on the flow velocity. Also, the effect of all three parameters depends on the mixture composition.
- Besides plot trends, the flow velocity and mixture composition also affect *SI* and *P* values. As the flow velocity increases, porosity and segregation in radial direction are reduced while segregation in vertical direction is increased. Porosity and segregation in radial direction are increased as the mixture contains more sinter, while segregation in vertical direction is highest when the mixture contains equal mass fractions of pellets and sinter.
- The pellet-sinter friction coefficients act together to affect segregation and porosity and can therefore not be changed independently.

Further research is required to explain why an increase in the pellet-sinter restitution coefficient reduces radial segregation while the opposite is true for the friction coefficients, regardless of the discharge height and mixture composition used. Similarly, understanding the effects in vertical direction requires more research especially since there is some dependence on the discharge height and mixture composition.

Declaration of competing interest

The authors declare that they have no known competing financial interests or personal relationships that could have appeared to influence the work reported in this paper.

Acknowledgements

This work was carried out as part of the "Industrial Dense Granular Flows" project, which received funding from the Dutch Research Council (NWO) in the framework of the ENW PPP Fund for the topsectors and from the Ministry of Economic Affairs in the framework of the "PPS-Toeslagregeling".

Appendix A. Effect of sample size on segregation index for other cases

A.1. Reference composition, other heights

(See Figs. A1 and A2).

A.2. Reference height, other compositions

(See Figs. A3 and A4).

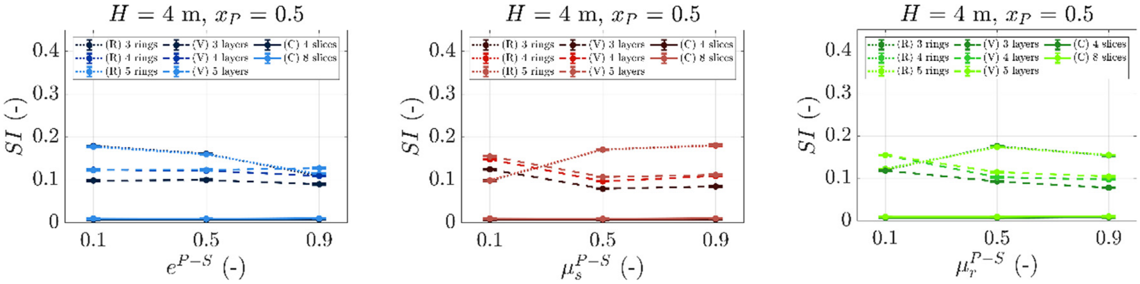

(a) (b) (c)

Fig. A1. Effects of (a) e^{P-S}, (b) μ_s^{P-S} and (c) μ_r^{P-S} on segregation in radial (R) and vertical (V) and circumferential (c) directions for $H = 4$ m and $x_P = 0.5$ calculated using different sample sizes. Error bars indicate the standard deviation of the segregation index based on three repetitions.

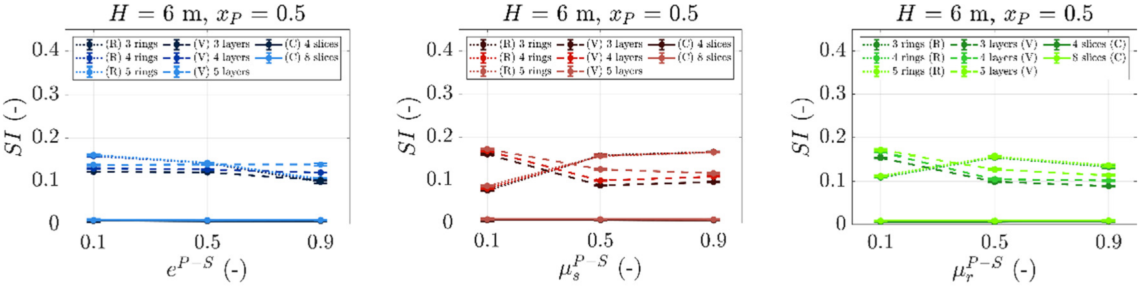

(a) (b) (c)

Fig. A2. Effects of (a) e^{P-S}, (b) μ_s^{P-S} and (c) μ_r^{P-S} on segregation in radial (R) and vertical (V) and circumferential (c) directions for $H = 6$ m and $x_P = 0.5$ calculated using different sample sizes. Error bars indicate the standard deviation of the segregation index based on three repetitions.

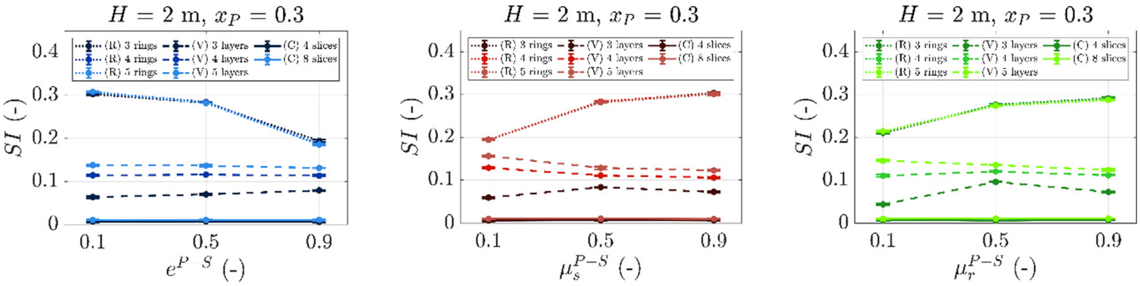

(a) (b) (c)

Fig. A3. Effects of (a) e^{P-S}, (b) μ_s^{P-S} and (c) μ_r^{P-S} on segregation in radial (R) and vertical (V) and circumferential (c) directions for $H = 2$ m and $x_P = 0.3$ calculated using different sample sizes. Error bars indicate the standard deviation of the segregation index based on three repetitions.

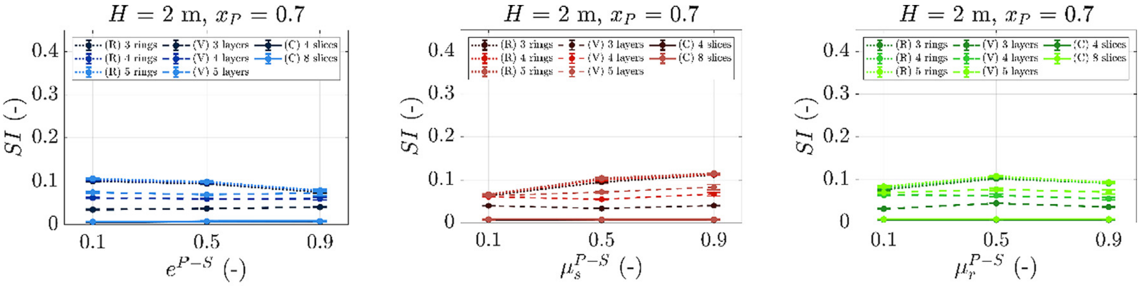

(a) (b) (c)

Fig. A4. Effects of (a) e^{P-S}, (b) μ_s^{P-S} and (c) μ_r^{P-S} on segregation in radial (R) and vertical (V) and circumferential (c) directions for $H = 2$ m and $x_P = 0.7$ calculated using different sample sizes. Error bars indicate the standard deviation of the segregation index based on three repetitions.

Appendix B. Interaction effects for other cases

B.1. Reference composition, other heights

Radial segregation
(See Figs. B1 and B2).

Vertical segregation

(See Figs. B3 and B4).

Porosity

(See Figs. B5 and B6).

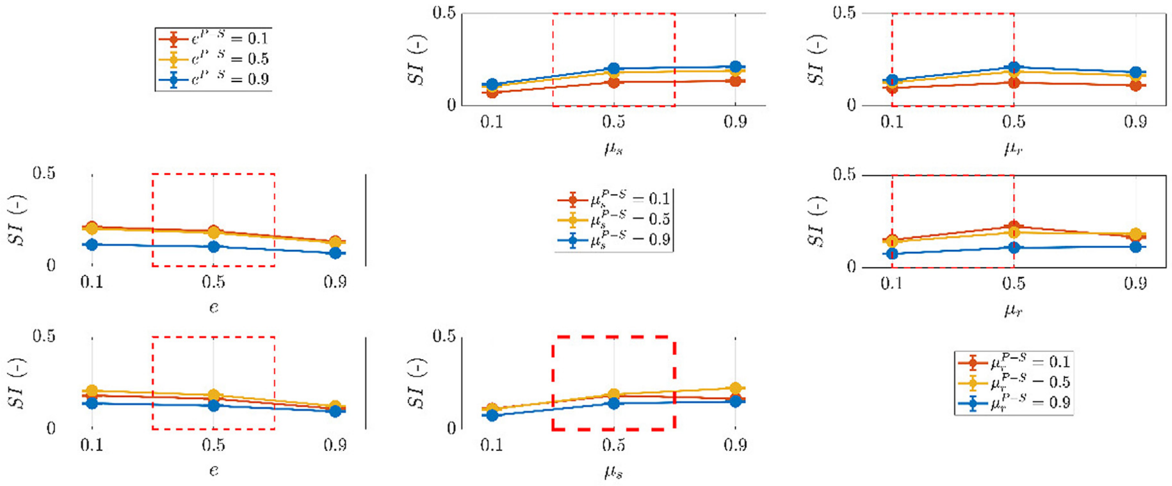

Fig. B1. Interaction effects of e^{P-S}, μ_s^{P-S} and μ_r^{P-S} on radial segregation for a discharge height of $H = 4$ meters. Error bars indicate the standard deviation of the segregation index based on three repetitions. (Thick) dashed boxes indicate (important) regions of interest.

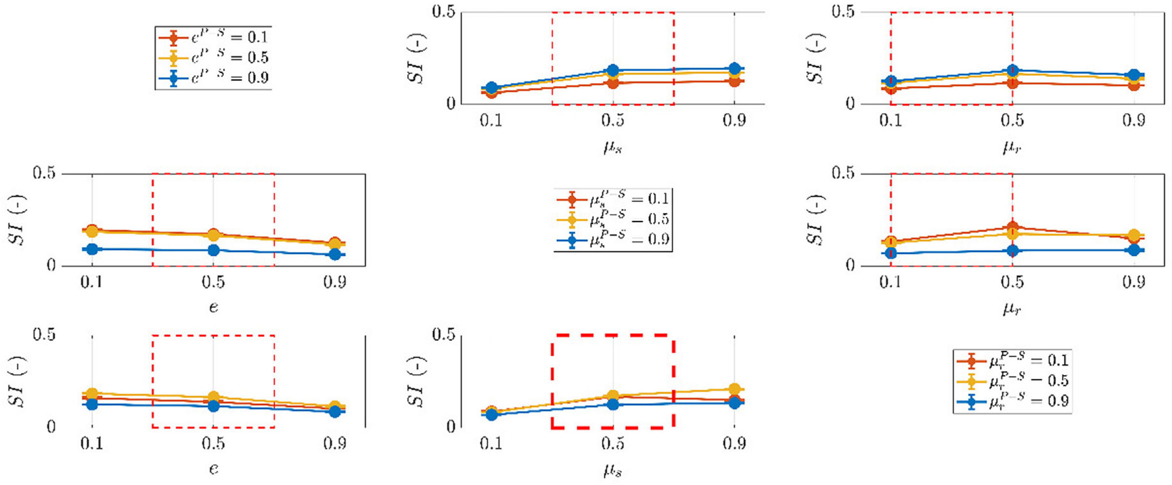

Fig. B2. Interaction effects of e^{P-S}, μ_s^{P-S} and μ_r^{P-S} on radial segregation for a discharge height of $H = 6$ meters. Error bars indicate the standard deviation of the segregation index based on three repetitions. (Thick) dashed boxes indicate (important) regions of interest.

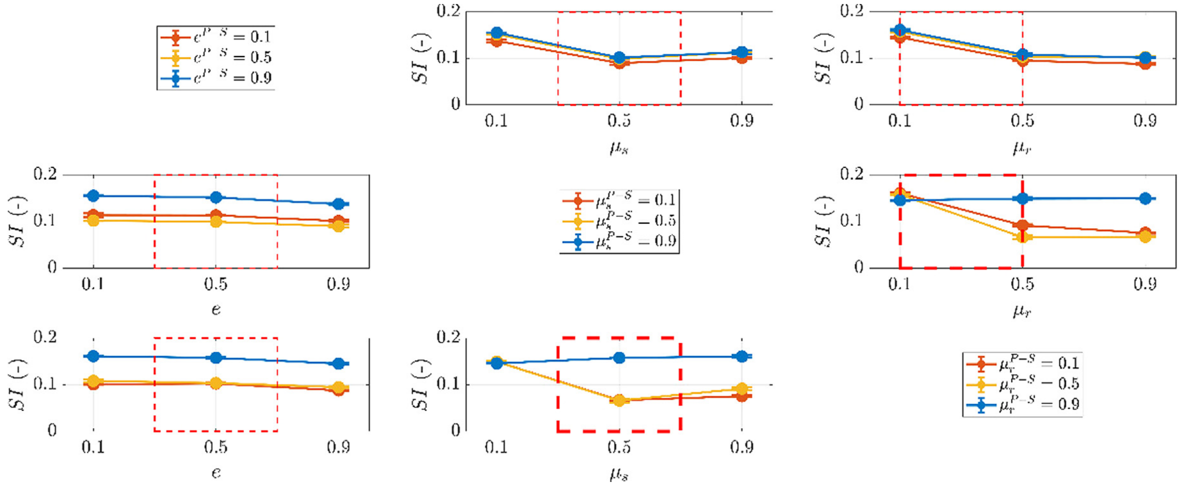

Fig. B3. Interaction effects of e^{P-S}, μ_s^{P-S} and μ_r^{P-S} on vertical segregation for a discharge height of $H = 4$ meters. Error bars indicate the standard deviation of the segregation index based on three repetitions. (Thick) dashed boxes indicate (important) regions of interest.

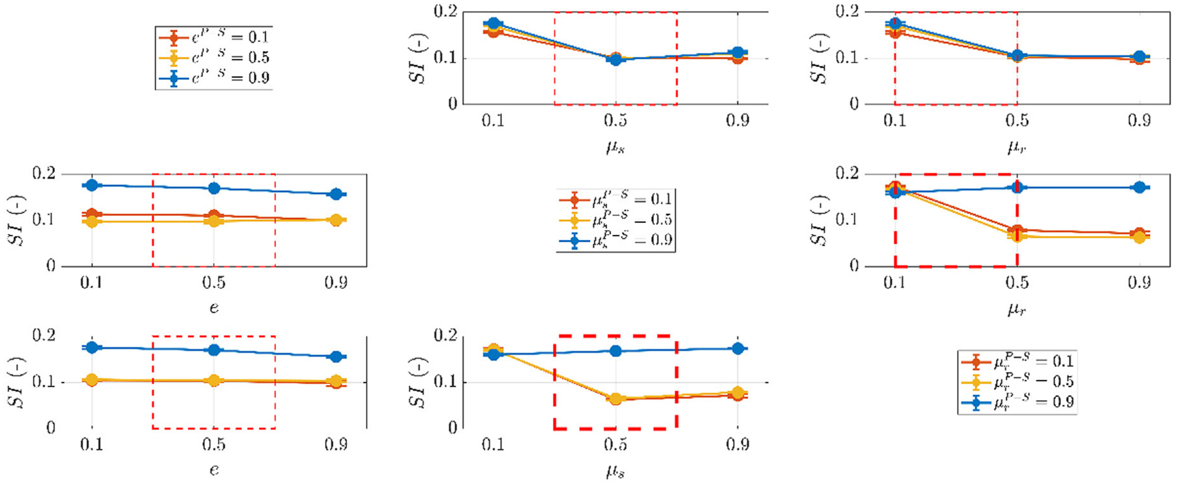

Fig. B4. Interaction effects of e^{P-S}, μ_s^{P-S} and μ_r^{P-S} on vertical segregation for a discharge height of $H = 6$ meters. Error bars indicate the standard deviation of the segregation index based on three repetitions.

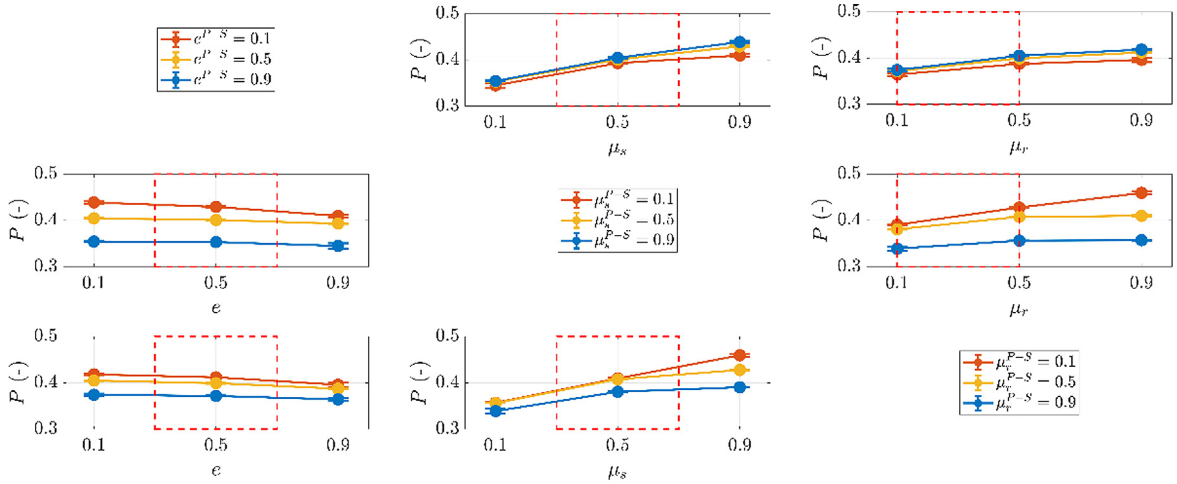

Fig. B5. Interaction effects of e^{P-S}, μ_s^{P-S} and μ_r^{P-S} on porosity for a discharge height of H = 4 m. Error bars indicate the standard deviation of the segregation index based on three repetitions. Dashed boxes indicate regions of interest.

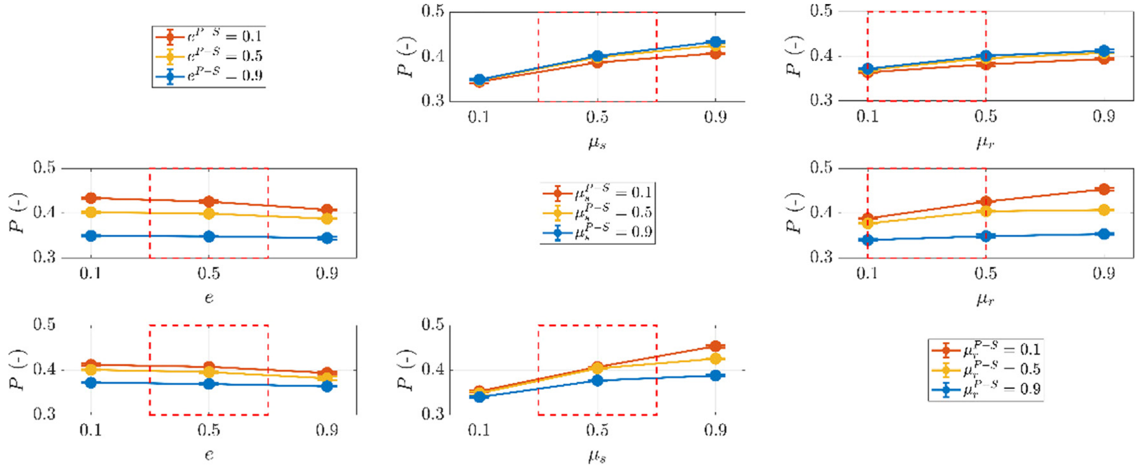

Fig. B6. Interaction effects of e^{P-S}, μ_s^{P-S} and μ_r^{P-S} on porosity for a discharge height of H = 6 m. Error bars indicate the standard deviation of the segregation index based on three repetitions. Dashed boxes indicate regions of interest.

B.2. Reference height, other compositions

Radial segregation

(See Figs. B7 and B8).

Vertical segregation

(See Figs. B9 and B10).

Porosity

(See Figs. B11 and B12).

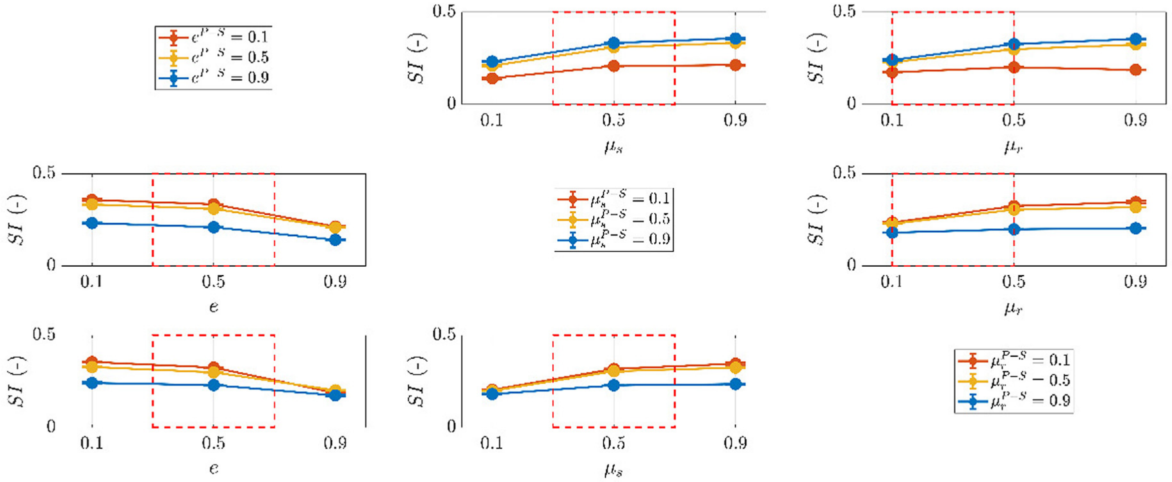

Fig. B7. Interaction effects of e^{P-S}, μ_s^{P-S} and μ_r^{P-S} on radial segregation when $x_p = 0.3$. Error bars indicate the standard deviation of the segregation index based on three repetitions. (Thick) dashed boxes indicate (important) regions of interest.

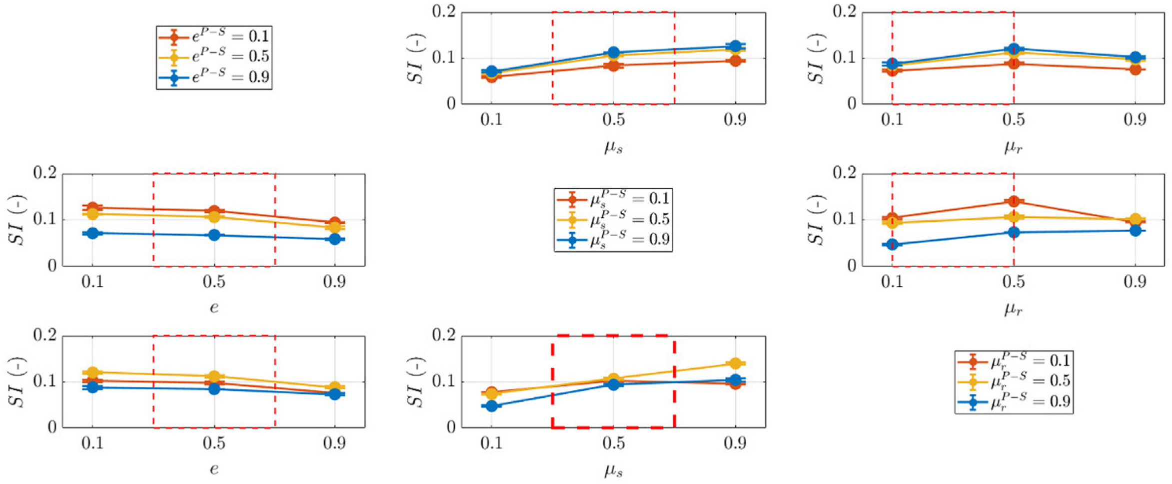

Fig. B8. Interaction effects of e^{P-S}, μ_s^{P-S} and μ_r^{P-S} on radial segregation when $x_p = 0.7$. Error bars indicate the standard deviation of the segregation index based on three repetitions. (Thick) dashed boxes indicate (important) regions of interest.

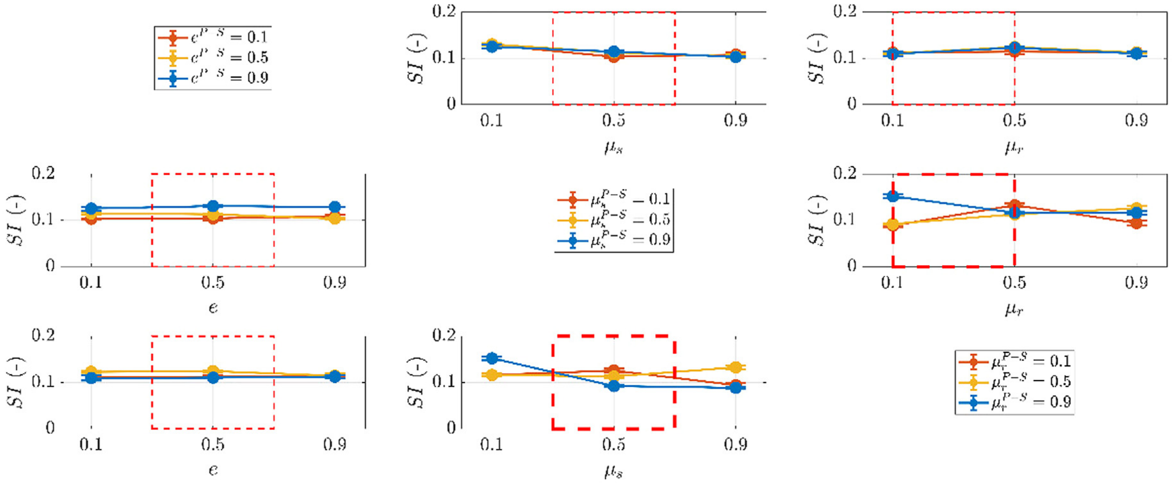

Fig. B9. Interaction effects of e^{P-S}, μ_s^{P-S} and μ_r^{P-S} on vertical segregation when $x_p = 0.3$. Error bars indicate the standard deviation of the segregation index based on three repetitions. (Thick) dashed boxes indicate (important) regions of interest.

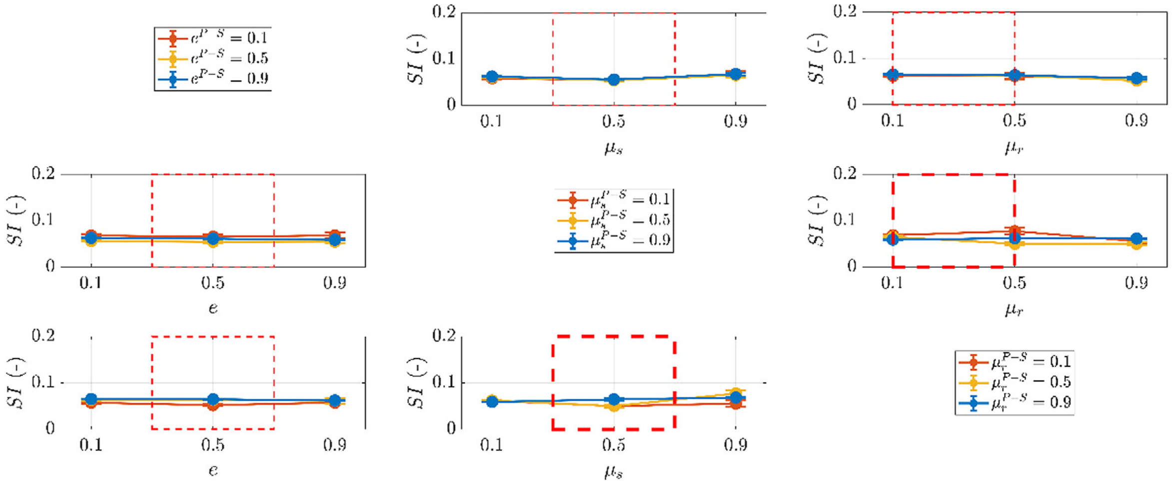

Fig. B10. Interaction effects of e^{P-S}, μ_s^{P-S} and μ_r^{P-S} on vertical segregation when $x_p = 0.7$. Error bars indicate the standard deviation of the segregation index based on three repetitions. (Thick) dashed boxes indicate (important) regions of interest.

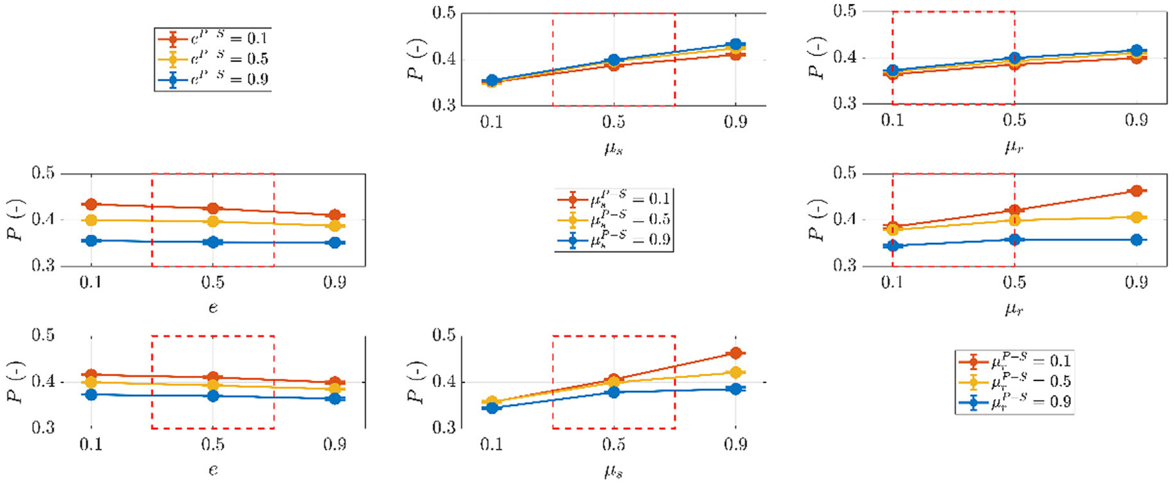

Fig. B11. Interaction effects of e^{P-S}, μ_s^{P-S} and μ_r^{P-S} on porosity when $x_p = 0.3$. Error bars indicate the standard deviation of the segregation index based on three repetitions. (Thick) dashed boxes indicate (important) regions of interest.

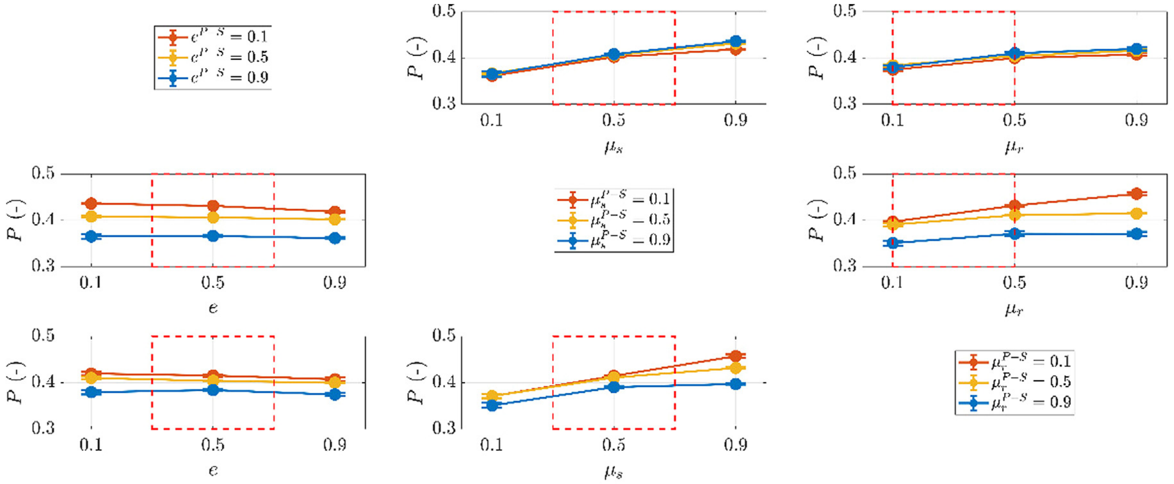

Fig. B12. Interaction effects of e^{P-S}, μ_s^{P-S} and μ_r^{P-S} on porosity when $x_p = 0.7$. Error bars indicate the standard deviation of the segregation index based on three repetitions. (Thick) dashed boxes indicate (important) regions of interest.

References

[1] C.K. Ho, S.M. Wu, H.P. Zhu, A.B. Yu, S.T. Tsai, Experimental and numerical investigations of gouge formation related to blast furnace burden distribution, Miner. Eng. 22 (11) (2009) 986–994.

[2] H. Li, H. Saxén, W. Liu, Z. Zou and L. Shao, ‘‘Model-Based Analysis of Factors Affecting the Burden Layer Structure in the Blast Furnace Shaft,” *Metals,* vol. 9, no. 9, 2019.

[3] C. Loo, L. Matthews, D. O'Dea, Lump ore and sinter behavior during softening and melting, ISIJ Int. 51 (2011) 930–938.

[4] B.D. Pandey, U.S. Yadav, Blast furnace performance as influenced by burden distribution, Ironmak. Steelmak. 26 (3) (1999) 187–192.

[5] Y. Yang, Y. Yin, D. Wunsch, S. Zhang, X. Chen, X. Li, S. Cheng, M. Wu, K.-Z. Liu, Development of blast furnace burden distribution process modeling and control, ISIJ Int. 57 (8) (2017) 1350–1363.

[6] M. Geerdes, R. Chaigneau and O. Lingiardi, Modern Blast Furnace Ironmaking: An Introduction, Fourth ed., H. T. Maarten Geerdes, Ed., IOS Press BV, 2020.

[7] R. Roeplal, Y. Pang, A. Adema, J. van der Stel and D. Schott, *Modelling of phenomena affecting blast furnace burden permeability using the Discrete Element Method (DEM) – A review,* vol. 415, 2023, p. 118161.

[8] P.A. Cundall, O.D.L. Strack, A discrete numerical model for granular assemblies, Géotechnique 29 (1) (1979) 47–65.

[9] R. D. Mindlin, ‘‘Compliance of Elastic Bodies in Contact,” *Journal of Applied Mechanics,* vol. 16, no. 3, pp. 259-268, 4 1949.

[10] J. Ai, J.-F. Chen, J. M. Rotter and J. Y. Ooi, Assessment of rolling resistance models in discrete element simulations, vol. 206, 2011, pp. 269-282.

[11] Z. Hong, H. Zhou, J. Wu, L. Zhan, Y. Fan, Z. Zhang, S. Wu, H. Xu, L. Wang and M. Kou, ‘‘Effects of Operational Parameters on Particle Movement and Distribution at the Top of a Bell-Less Blast Furnace Based on Discrete Element Method,” *steel research international,* vol. 92, 8 2020.

[12] M.A.J. Holmes, D.J. Penney, N.P. Lavery, S.G.R. Brown, A numerical investigation assessing the symmetry of burden charging in a blast furnace using different chute designs, Ironmak. Steelmak. 45 (6) (2018) 551–559.

[13] M. Kou, J. Xu, S. Wu, H. Zhou, K. Gu, S. Yao, B. Wen, Effect of cross-section shape of rotating chute on particle movement and distribution at the throat of a bell-less top blast furnace, Particuology 44 (2019) 194–206.

[14] K. Zhou, Z. Jiang, D. Pan, W. Gui and J. Huang, ‘‘Influence of Charging Parameters on the Burden Flow Velocity and Distribution on the Blast Furnace Chute Based on Discrete Element Method,” *steel research international,* vol. 93, no. 1, 2021.

[15] W. Xu, S. Cheng, Q. Niu, W. Hu and J. Bang, ‘‘Investigation on the uneven distribution of different types of ores in the hopper and stock surface during the charging process of blast furnace based on discrete element method,” *Metallurgical Research & Technology,* vol. 116, p. 314, 1 2019.

[16] J. Chen, H. Zuo, Y. Wang, Q. Xue, J. Wang, DEM simulation of burden circumferential distribution of blast furnace with parallel hoppers, Metall. Mater. Trans. B 53 (6) (2022) 3793–3804.

[17] S. Liu, Z. Zhou, K. Dong, A. Yu, D. Pinson and J. Tsalapatis, ''Numerical Investigation of Burden Distribution in a Blast Furnace,'' vol. 86, 2015, pp. 651-661.

[18] C. Li, T. Honeyands, D. O'Dea and R. Moreno-Atanasio, ''The angle of repose and size segregation of iron ore granules: DEM analysis and experimental investigation,'' vol. 320, 2017, pp. 257-272.

[19] D.K. Chibwe, G.M. Evans, E. Doroodchi, B.J. Monaghan, D.J. Pinson, S.J. Chew, Charge material distribution behaviour in blast furnace charging system, Powder Technol. 366 (2020) 22–35.

[20] S. Wei, H. Wei, H. Saxen and Y. yu, ''Numerical Analysis of the Relationship between Friction Coefficient and Repose Angle of Blast Furnace Raw Materials by Discrete Element Method,'' vol. 15, 2022, p. 903.

[21] D. Schott, W. Vreeburg, C. Molhoek and G. Lodewijks, ''Granular Flow to a Blast Iron Ore Furnace: Influence of Particle Size Distribution on Segregation of a Mixture,'' Traffic and Granular Flow '15, pp. 621–628-621–628, 2016.

[22] H. Kruggel-Emden, S. Wirtz and V. Scherer, A study on tangential force laws applicable to the discrete element method (DEM) for materials with viscoelastic or plastic behavior, vol. 63, 2008, pp. 1523-1541.

[23] (DHPC), Delft high Performance Computing Centre, *DelftBlue Supercomputer Phase 1*, Delft, 2022.

[24] A. Chakrabarty, R. Biswas, S. Basu, S. Nag, Characterisation of binary mixtures of pellets and sinter for DEM simulations, Adv. Powder Technol. 33 (1) (2022) 103358.

[25] C. Thornton, C.W. Randall, Applications of theoretical contact mechanics to solid particle system simulation, Micromech. Gran. Mater. 20 (1988) 133–142.

[26] Altair EDEM, ''EDEM Simulator Settings,'' [Online]. Available: https://help.altair.com/EDEM/Simulator.htm.

[27] J. M. Boac, M. E. Casada, R. G. Maghirang and J. P. Harner III, 3-D and Quasi-2-D Discrete Element Modeling of Grain Commingling in a Bucket Elevator Boot System, vol. 55, St. Joseph, MI: ASABE, 2012, pp. 659-672.

[28] P. Bhalode, M. Ierapetritou, A review of existing mixing indices in solid-based continuous blending operations, Powder Technol. 373 (2020) 195–209.

[29] H. Li, J.J. McCarthy, Cohesive particle mixing and segregation under shear, Powder Technol. 164 (1) (2006) 58–64.

[30] M. Cho, P. Dutta, J. Shim, A non-sampling mixing index for multicomponent mixtures, Powder Technol. 319 (2017) 434–444.

[31] Q. Song, Effect of nut coke on the performance of the ironmaking blast furnace, Delft Academic Press, Delft, 2017.

[32] J. Antony, ''4 - A Systematic Methodology for Design of Experiments,'' Second Edition ed., J. Antony, Ed., Oxford, Elsevier, 2014, pp. 33-50.

[33] J. von Seckendorff and O. Hinrichsen, Review on the structure of random packed-beds, vol. 99, 2021, pp. S703-S733.

[34] H. Wei, X. Tang, Y. Ge, M. Li, H. Saxén, Y. Yu, Numerical and experimental studies of the effect of iron ore particle shape on repose angle and porosity of a heap, Powder Technol. 353 (2019) 526–534.

[35] Y. Yu and H. Saxén, ''Flow of Pellet and Coke Particles in and from a Fixed Chute,'' vol. 51, 2012, p. 7383–7397.

[36] H. Mio, S. Komatsuki, M. Akashi, A. Shimosaka, Y. Shirakawa, J. Hidaka, M. Kadowaki, S. Matsuzaki, K. Kunitomo, Effect of Chute angle on charging behavior of sintered ore particles at bell-less type charging system of blast furnace by discrete element method, ISIJ Int. 49 (4) (2009) 479–486.